8-2020

Parametric Study of Infrared Imaging Based Breast Cancer Detection Program

Carlos B. Gutierrez
cg9804@rit.edu

ROCHESTER INSTITUTE OF TECHNOLOGY

PARAMETRIC STUDY OF INFRARED IMAGING BASED BREAST CANCER DETECTION PROGRAM

by

Carlos B Gutierrez

A Thesis Submitted in Partial Fulfillment of the Requirements for the Degree of
Master of Science in Mechanical Engineering

Supervised by

Dr. Satish Kandlikar
Department of Mechanical Engineering
Kate Gleason College of Engineering
Rochester Institute of Technology
Rochester, NY
August 2020

PARAMETRIC STUDY OF INFRARED IMAGING BASED BREAST CANCER DETECTION PROGRAM

By: Carlos B Gutierrez

A Thesis Submitted in Partial Fulfillment of the Requirements for the Degree of Master of Science in Mechanical Engineering

Department of Mechanical Engineering
Kate Gleason College of Engineering
Rochester Institute of Technology
Rochester, NY
August 2020

Approved By:

Dr. Satish Kandlikar
Advisor – Department of Mechanical Engineering

Dr. Iris Rivero
Examiner – Department of Industrial and Systems Engineering

Dr. Michael Richards
Examiner – Department of Biomedical Engineering

Dr. Michael Schrlau
Dept. Representative – Department of Mechanical Engineering

Acknowledgements

I would like to thank Dr. Satish Kandlikar for allowing me to join the lab and this project as well as for all his support, advice, and kindness. He has made it possible for me to pursue my dreams by allowing me to be part of his lab. He has inspired and pushed me throughout the time I have worked in the lab and on this project. I feel extremely grateful working under such a revolutionary and amazing researcher. I would also like to thank my lab mates, past and present, for being such inspirations and an amazing support group. I would like to especially thank Dr. Alyssa Owens for all her guidance in the project and for all she does for the lab.

Thank you to my committee members for being part of this journey and advising me through the initial stages of this thesis. I am grateful for all their support and I hope to continue working with them as I continue my studies and this project as a PhD student.

I would like to thank my family for their constant support throughout the years. Most importantly, I would like to thank my parents for all the sacrifices they made to get me where I am today and for always loving and supporting me. There are no words that can express the gratitude I have for all they have done so that I may go college to get my Bachelors degree and now my Masters degree despite the hurdles. My father's lost battle with cancer and his natural tendencies to help others are my main inspirations and driving force in working in this project.

Lastly, I would like to thank Viktoria for her friendship and never giving up on me as well as being there at the lowest times of my life. If it were not for her believing in me and pushing me in those times, I would not have even applied to RIT and gotten through my first semester after my father's death.

All published and copyrighted figures, tables, or representations thereof, are cited and included with permission.

Abstract

Breast cancer is one of the most common cancers among women and is responsible for over 41,000 lives every year in the US according to The American Cancer Society. Current screening and imaging methods such as mammography, breast magnetic resonance imaging, and breast ultrasound imaging have helped in improving survival rate when the cancer is detected at an early stage. The problems with these techniques include: low sensitivity, patient discomfort, invasiveness, and cost. Due to current advancements in infrared and computational technologies, infrared thermography has been utilized as a noninvasive adjunctive screening modality. A computerized approach using infrared imaging (IRI) has been recently developed at RIT in collaboration with Rochester General Hospital for breast cancer detection and image localization. The parameters used in this simulation have been selected based on limited information available in the literature. This study focuses on analyzing the effects of different tissue thermal parameters used in the simulation on the accuracy of prediction. Thermal conductivity and perfusion rate are systematically varied, and their effects are presented by comparing simulated images with the actual infrared images captured from a biopsy-proven breast cancer patient. The results indicate a strong influence of perfusion rate within the breast tissue surrounding the tumor on heat transfer within the breast. This study is expected to help in proper selection of thermal properties while conducting the simulations. Future directions for research are also presented.

Table of Contents

List of Figures

List of Tables

Nomenclature

δ_{kx}	Frequency shift in the x-direction
δ_{ky}	Frequency shift in the y-direction
λ_e	Effective thermal conductivity, W/cm•ºC
ρ_b	Density of blood, kg/m^3
ρ_t	Density of tissue, kg/m^3
$\phi_{m,n}$	Phase shift information
ω	Perfusion rate, 1/s
ω_b	Blood perfusion rate, 1/s
ω_h	Blood perfusion rate of healthy tissue, 1/s
ω_q	Perfusion rate at q, 1/s
ω_t	Blood perfusion rate of tumorous tissue, 1/s
ω_x	Frequency sample in the x-direction
ω_y	Frequency sample in the y-direction
c_b	Specific heat of blood, J/kg•ºC
c_t	Specific heat of tissue, J/kg•ºC
d_t	Tumor diameter, m
DT	Doubling time
f	Function
F	Continuous Fourier transform of f
F_k	Discrete Fourier transform of f
$F_{m,n}$	Samples of the alias free CFT of the high-resolution signal

$G_{m,n}$	Values of the DFT of each signal
h	Heat transfer coefficient, W/m^2•K
$I_{i,j}$	Intensity value at the pixel index (i,j)
I_{max}	Maximum intensity value
I_{min}	Minimum intensity value
k	Signal number or thermal conductivity, W/m•K
k_h	Thermal conductivity of healthy tissue, W/m•K
k_p	Thermal conductivity at p, W/m•K
k_t	Thermal conductivity of tissue or tumor, W/m•K
L_x	Desired increase in resolution from the original data to the final reconstructed data in the x-direction
L_y	Desired increase in resolution from the original data to the final reconstructed data in the y-direction
m	discrete variable in x-direction
m_0	Initial discrete variable in the x-direction
M	Sample point in x-direction
n	discrete variable in y-direction
$\boldsymbol{n}$	Normal vector
n_0	Initial discrete variable in the y-direction
N	Sample point in y-direction
$N \times M$	Size of temperature matrix
q^*	Metabolic heat production, W/cm^3
q_m	Metabolic heat generation rate, W/m^3
Q_h	Metabolic activity of healthy tissue, W/m^3

Q_t	Metabolic activity of tumorous tissue, W/m^3
S_x	Shifts in the x-direction
S_y	Shifts in the y-direction
t	Time, s
T	Temperature, ºC
T_a	Artery temperature, ºC
T_c	Core body temperature, ºC
$T_{i,j}$	Temperature at the pixel index (i,j), ºC
T_{IRI}	IRI image temperature, ºC
T_{max}	Maximum temperature, ºC
T_{min}	Minimum temperature, ºC
T_{num}	Computed temperature image temperature, ºC
T_t	Tissue temperature, ºC
T_x	Sample period in the x-direction
T_y	Sample period in the y-direction
T_∞	Ambient temperature, ºC
u	Frequency variable in the x-direction
v	Frequency variable in the y-direction
x_{max}	Maximum x value in computational domain, m
x_{min}	Minimum x value in computational domain, m
x_t	x coordinate of tumor, m
y_{max}	Maximum y value in computational domain, m

y_{min} Minimum y value in computational domain, m

y_t y coordinate of tumor, m

z_{max} Maximum z value in computational domain, m

z_{min} Minimum z value in computational domain, m

z_t z coordinate of tumor, m

1 Introduction

In recent years, the advancement in cancer research has been greatly improved by the advancement of technology. There have been huge breakthroughs in medical imaging research for new techniques to test for breast cancer. Unfortunately, most techniques are invasive or inflict physical discomfort for patients such as radioactive particle injections or breast compression [1]. Noninvasive techniques such as Optical Imaging Tests [2], Photoacoustic Imaging [3], and Thermoacoustic Imaging [4] have been studied, but have not been fully implemented in the clinical setting. Similarly, the use of breast thermography as a feasible adjunctive breast cancer screening modality has been investigated in conjunction with computational techniques.

1.1 Breast Cancer and Screening Modalities

The breast is composed of a tissue layer that goes over the chest, or pectoral muscle that consists of the lobules, ducts, and fatty tissue as well as containing blood vessels and lymph nodes [5, 6]. Breast cancer is a disease where abnormal growth of mutated cells, or tumors, typically starts in the ductal or lobular region of the breast. The most common types of breast cancer are found in the ducts (approximately 75% of breast cancers) such as ductal carcinoma in situ (DCIS) and invasive ductal carcinoma (IDC). One of the least common types occur at the lobules (approximately 10-15% of breast cancers) such as invasive lobular carcinoma (ILC) [5, 6]. Lobular carcinomas such as lobular carcinoma in situ (LCIS) and atypical lobular hyperplasia (ALH) are subtypes of lobular neoplasia, which are noncancerous diseases that show abnormal cells and raise risk of obtaining breast cancer in the future [6].

According to the National Breast Cancer Foundation [7] and American Cancer Society [1], breast cancer is one of the most common cancers amongst women, taking hundreds of thousands of lives every year, with over 41,000 lives lost every year in the US alone. Early detection of breast cancer

is crucial for improved survival rates, which can be up to 99% if detected early enough and if the cancer is in its earlier stages [7]. Medical screening and imaging have played a huge role in the detection and diagnosis of breast cancer. Common screening and imaging techniques are mammography (MMG), breast magnetic resonance imaging (MRI), and ultrasound imaging.

1.1.1 Mammogram (MMG)

In MMG, patients have each of their breasts compressed by a machine which captures low dose x-rays of each breast tissue. The breast compression spreads the tissue out to give a better picture and to use less x-ray radiation. The images are usually taken at two different angles. However, there is newer type of MMG called digital breast tomosynthesis, in which a machine compresses the breast once and captures multiple mammograms that are stitched into a three-dimensional (3D) image with the aid of a computer [1]. The problems with MMG come with the discomfort from the machine compressing the breast before taking any images, as well as when testing patients with dense breast tissue. Since these tissues obscure the tumors, they become difficult to distinguish from surrounding regions. This can lead to a false-negative or false-positive result. Both false-negative and false-positive results create psychological and financial issues due to further testing that is needed, depending on the individual outcome. In 2015, the accuracy of diagnosis through mammography was about 78% for women under 50 and about 83% for women over 50 [8].

1.1.2 Breast Ultrasound

Breast ultrasound imaging is the technique of using sound waves to create images of the inside of the breast with the aid of computer software. This technique can show changes in the breast regardless of the breast tissue density of the patient, as well as differentiate between a cyst and tumor [1]. Although this technique does not expose patients to radiation, is widely available, and

is more accurate and sensitive than MMG, breast ultrasound does not cater specifically to patients 50 years and older [1, 9]. According to a study done on 326 breast tumors, ultrasound had an accuracy of 84% and sensitivity of 82% compared to MMG which had an accuracy of 81% and sensitivity of 49% in detecting and imaging the tumors [9].

1.1.3 Breast Magnetic Resonance Imaging

Breast MRI is an imaging technique that takes detailed picture slices of the inside of the breast with the use of a strong magnet and radio waves. It is a useful technique to detect cancers on patients who have denser breast tissue and other types of diseases, but it is more commonly used to screen high-risk patients or further diagnosis prior to surgical resection. Although breast MRIs are not as uncomfortable as MMG, the procedures can still be invasive as the majority of breast MRIs are enhanced by injecting contrast materials into the patient during or before imaging [1, 10]. MRIs are considered more sensitive than both mammography and ultrasound imaging but are not recommended without a combination of screening methods [11, 12]. There have been studies which proved that the sensitivity of MRI is slightly better than MMG and ultrasound screening combination; however, it is only a slight increase. The expensiveness of testing outside of a high-risk patient population makes it difficult to use as a screening tool [12, 13].

1.2 Thermography

Thermography is a technique that is used to find temperature differences, patterns, or distribution on the surface of an object. These temperatures are measured using an infrared (IR) camera, which captures IR radiation emitted from the surface of the object and transmits it as a thermal image, or infrared image. IR thermography or infrared imaging (IRI) has a large range of usability such as finding heat losses in buildings, monitoring of mechanical and electrical systems, and a medical instrument in the health profession [14]. Biomedical studies have utilized IR thermography to

conduct research of the lung and large intestines, diseases related to the extremities, plastic and reconstruction surgery, and many others [15, 16, 17]. IR thermography has also been used for biochemical studies of complementary imaging systems and contrast agents, as well as computational psychophysiological studies in the neurosciences [18, 19]. An example of the applications of IR thermography is shown in Fig. 1. Breast cancer thermography has been studied as a breast cancer screening modality, which will be further discussed in the literature review chapter.

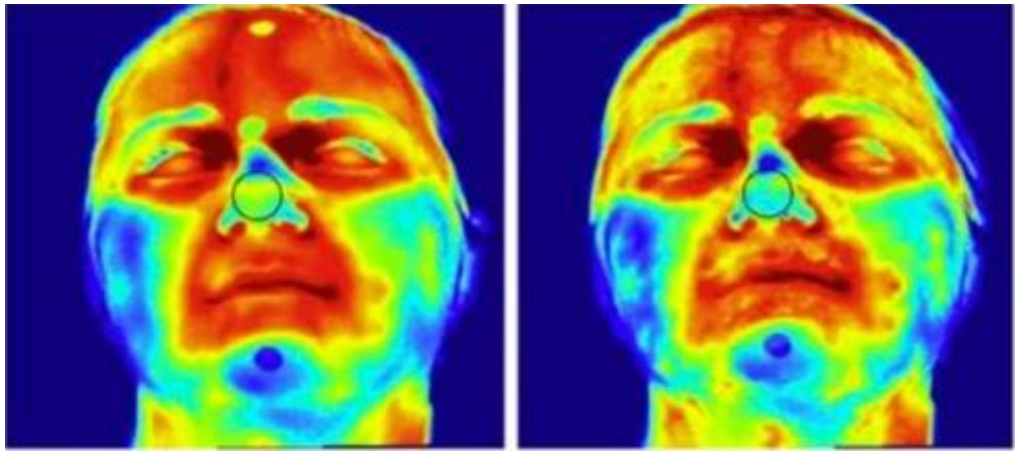

Figure 1: *The right image shows a temperature deviation from the left image when acoustic stimulus is introduced to a person as studied by Cardone and Merla [19], reproduced with permission.*

1.3 Computerized IRI Program for Breast Cancer Detection

Through a collaborative study between Rochester Institute of Technology (RIT) and Rochester General Hospital (RGH) a computerized IRI program for the detection and localization of breast cancers was created [20, 21]. This program utilized a method for creating patient-specific digital breast models from the MRI images, a numerical simulation of the heat transfer within the breast, image processing techniques, and an inverse heat transfer approach [21, 22, 23]. Gonzalez-Hernandez et al. [21, 22] created a method to generate patient-specific digital models of female breasts in the prone position using MRI images and image processing techniques. They conducted

numerical thermal simulations of a breast tumor on the models using Pennes' bioheat equation [24] and Gautherie's observations of thermal characteristics of breast tumors [25, 26], which will be further discussed in the literature review chapter.

Using this method to create patient-specific digital breast models and simulating a cancerous breast, an inverse heat transfer approach was used with IRI images to detect and localize a tumor on biopsy-proven patients [20, 21, 23, 27]. This method obtained computed temperature images of the simulated model and compared these images with corresponding IRI images through image registration and an iterative inverse heart transfer algorithm known as the Levenberg-Marquardt algorithm [23]. This method was further validated and is a preliminary basis to an ongoing clinical study of using IRI as an adjunctive screening modality [27]. These works utilized bioheat modeling and image processing to create a method that detects and localizes a tumor. They used thermal properties depending on the type of breast tissue from the pathology reports.

2 Literature Review

There has been an extensive body of research on the use of thermography as a breast cancer screening modality. With the advancement of computational technology and methods, many previous studies have been recently re-explored. This chapter will focus on previous and current breast cancer thermography research, bioheat transfer analytic and computational models, and image processing and computer graphics techniques.

2.1 Breast Cancer Thermography

As computational technology advanced, breast cancer research incorporated these advancements for developing noninvasive techniques for screening and diagnostic purposes. Breast cancer thermography has been a controversial topic since the early 1970s due to a lack of clear protocol

and inadequate clinical validation, but there has been a current increase of interest in this research area, especially after recent technological breakthroughs through patient-specific models. In this section, some previous literature on thermography, its advancements, and the current status will be discussed.

2.1.1 Early IR Thermography

Lawson [28] was one of the first researchers that questioned whether there is a correlation between breast cancer tumors and the heat they release onto the body. He physically took temperature measurements off a patient's skin to conduct his study using thermocouples. This research, as well as others similar to it, began the wave of research on the use of breast thermography as a possible screening technique. In these studies, researchers used tools such as a liquid crystal thermogram, or thermal sensors to measure the skin temperature. Researchers such as Isard et al. [29], Stark and Way [30], Jones et al. [31], Moskowitz et al. [32], and Williams et al. [33] used thermal sensors as their thermography tools to conduct their studies. Other researchers, such as Moskowitz et al. [34], did their studies using liquid crystal thermography, which is a method that showed temperature changes of the surface when in contact with film of liquid crystals [34]. Throughout the 1970s up until 1990, liquid crystal thermography was a comparable tool to thermal sensors like IR sensors [35]. Some researchers, such as Gautherie [25, 26], utilized both thermography techniques in their study.

In 1977, Dodd [36] conducted a status report on the use of thermography, ultrasound, and mammography in breast cancer detection. In his work, Dodd [36] studied the possibility of thermography and ultrasound "as replacements for or supplements to the mammographic examination" [36]. He concluded that "thermography finds its greatest use as an adjunct to mammography and physical examination; it should not be used as the sole modality in a screening

program" [36]. Further research conducted on thermography emphasized that this technique was not to be used as a clinical screening process, but it should not be ruled out as a possibility for the future. In 1985, Moskowitz [37] conducted a review on previous work done by him, his colleagues, and other researchers on thermography as a breast screening technique where he concluded the same outcome, but with suggestions on how to improve future studies. Regardless of the technique used to get thermography measurements, most of the researchers concluded that thermography was not a viable standalone technique for breast cancer detection. Many researchers, such as Moskowitz [37], believed that further studies were needed to be pursued in this realm of research.

Although there was backlash on the use of thermography for breast cancer research, Gautherie [25] conducted a 14-year-long clinical and fundamental study to find thermopathological correlations of breast tumors using thermography. In the study, a mass screening was implemented on about 58,000 symptomatic women where all patient information and history was obtained, and each patient underwent physical, thermographic, and mammographic examination. Some patients who were diagnosed with breast cancer, 3,034 patients, received treatment and/or operation, and others either refused treatment or were not able to get treatment due to other diseases. These two groups were selected to obtain intramammary measures where both tumoral and peritumoral temperature measurements as well as thermal flows were obtained. The first group, who received treatment, went through a single examination between diagnosis and the beginning stages of treatment. The second group went through this examination multiple times throughout the natural evolution of the cancer.

These examinations were done using a sterile 8mm diameter fine-needle thermoelectric probe that was implanted into the cancerous breast and contralateral healthy breast. Due to the low thermal capacity of the needle, there was no disruption of the local temperature and thermal flow.

Histological studies as well as experimentation on rheoelectrical phantom models that simulated the breast structure, thermal characteristics, external heat exchange, and vascularity, showed this to be the case. This examination was implemented through an ethical clinical agreement and was limited by the length and fragility of the needle as well as the tumor type, which in turn allowed for only 147 patients to be examined. Using the phantom models, clinical data, and the mathematical correlations between the conservation of steady state heat and electrical energy, a mathematical heat transfer model was obtained. The model showed the correlation between the geometric properties of the breast and tumor, and "thermal parameters involved with the heat transfer from the tumor to the surrounding tissues" [25].

Also, in the study, IR and liquid crystal thermography were utilized to conduct qualitative analysis on thermovascular patterns on any region of interest on the surface of the breast. Quantitative evaluations of temperature differences in local areas of hyperthermia were also obtained and compared with a reference, such as the same region in the contralateral breast. Complementary to this, radiotelethermometric recordings and rhythmometric analysis of skin temperature were obtained using thermistors with an oscillator to proportionally match frequencies to skin temperature. The location of these thermistors was dependent on the findings from the thermography examination. The evaluation of the measurements obtained was done through statistical analysis using a computer program and made it possible to record circadian or circatrigintan rhythms and other similar cycles.

The results obtained from the physical and thermographic study show the thermal effects of the tumor through the changes in temperature and thermal flow. Not only did Gautherie physically obtain the temperature of intramammary tissue and tumor, but he also obtained the effective thermal conductivity of the two. The effective thermal conductivity that was measured involved

both the tissue conduction and the convection due to capillary vessels, assuming they are isotropic, and the values ranged depending on breast density. The breast density was classified into three categories: fat, fibrous, or glandular, with fat being the least dense and glandular being the densest. In this study, the results showed that both the temperature and effective thermal conductivity were much higher than that of the contralateral healthy breast. He observed that, in a healthy breast, the temperature gradually increases the deeper you go into the breast tissue, but a major increase in temperature can be seen when a tumor is present. Similarly, the effective thermal conductivity is approximately constant in a healthy breast while the introduction of a tumor gives an abnormal increase in its vicinity. This increase in values was correlated to an increase of blood supply from the tumor region, or hypervascularization. This is due to the physiopathological concept that an increase in blood supply from the tumor is due to an increase in metabolism which in turn gives an increase in local heat production. From these examinations, it can be concluded that a tumor can be considered a heat source with an increase in vasculature and thermal flow that transfers heat to the surrounding tissue. This means that the heat transfer is not only from the effective thermal conductivity, but from the convection of larger vessels which depends on the metabolic activity that produces greater blood flow.

This metabolic heat production (q^*) was further evaluated throughout the period of tumor evolution with the rate of growth, the doubling time (DT), recorded for 84 patients that had tumor sizes of 0.9-3.8 cm. It was observed that during growth the metabolic heat production remained approximately constant regardless of circulatory and histological changes and was related to the DT by the hyperbolic law, as shown in Fig. 2. This meant that the faster the tumor grows, the more heat is generated and similarly the slower it grows, the less heat is generated. As shown by the figure, the DT ranged from 49-676 days with metabolic heat production ranging from $3.8 -$

68×10^{-3} W/cm^3. For fast growing tumors the DT $\leq$ 150 days have a metabolic heat production $q^* \geq 20 \times 10^{-3}$ W/cm^3, and for slow growing tumors the DT $\geq$ 250 days have a metabolic heat production $q^* \leq 10 \times 10^{-3}$ W/cm^3. Also, it was observed this relationship between DT and metabolic heat production applied to tumors smaller than 4 cm. According to Gautherie, this correlation between DT and metabolic heat production can be a helpful tool to obtaining DT by knowing the metabolic heat production at the time of diagnosis.

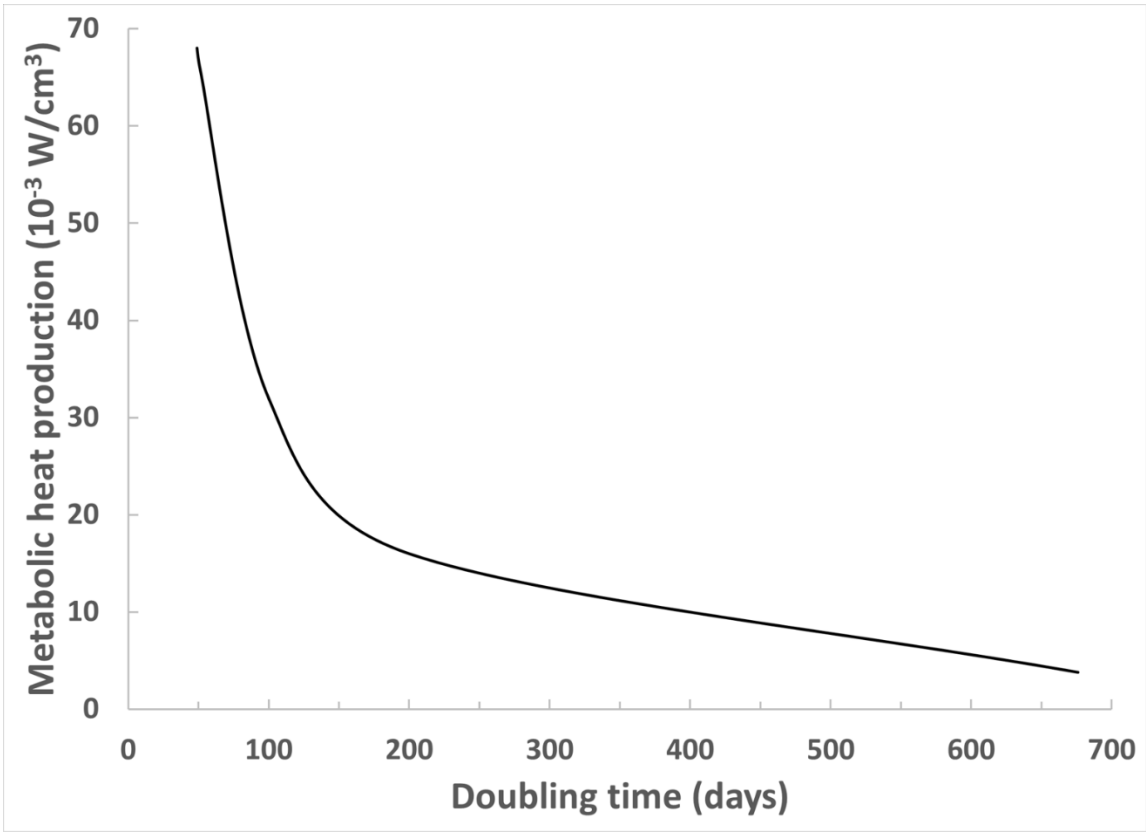

Figure 2: *Hyperbolic law relation between metabolic hear production and the doubling time of tumor volume for patients with and without lymph node metastases; redrawn from ;* redrawn from *Gautherie [25].*

In all these previous studies, one of the issues with thermography as a screening technique was due to low sensitivity. Williams et al. [33] obtained a 61% sensitivity in their research, which did not compete with the sensitivity of MMG at the time which was 78% to 94%. Another issue with

these studies was the lack of understanding of the thermography results as well as the lack of finding a correlation between tumor growth and thermal properties. However, Gautherie's study shows the usefulness of screening for breast cancer through a thermopathological approach using thermography [25]. As Gautherie once said, "[it] must also be recognized that further research on the subject of thermobiology of tumors should be undertaken" [26]. Thermography was approved by the U.S. Federal Drug Administration (FDA) as an adjunctive screening modality, but has not been approved as a stand-alone method [38].

2.1.2 IR Thermography

Current cancer research and technological advancements have also advanced our understanding of thermography as a screening technique. After the 1990s, research leaned towards IR technology as a tool to conduct thermography studies especially with the improvements made to IR cameras pixel resolution. In 2013, Sella et al. [39] conducted research using IRI as a method to study the metabolic signatures associated with breast tumors. They created their own prototype three-dimensional infrared imaging system (3DIRI) which was used with a multiparametric computer analysis tool to assess the risk of having a malignant tumor present in the breast. Their study obtained a 90.9% sensitivity value, which competes with common screening sensitivity values. EtehadTavakol et al. [40] also conducted research on thermography with IRI by associating certain cases, or classes, such as malignant, benign and normal, to higher order spectral features. This was done by taking IRI images of the breasts and extracting information, such as where the outer boundaries are based on the edges of the images, the hotspot regions, and Radon projections, which were used by a statistical method, done in a bi-frequency space called the bispectral invariant, to make classifications from these extractions.

Work done by Sella et al. [39], EtehadTavakol et al. [40], and many others shows the promise of IR technology as a useful tool for thermography breast cancer screening, but there are some, such as Collett et al. [41], who do not support IRI as a screening or diagnostic tool. This might be due to the lower sensitivity values obtained by Collett et al. [41]. They obtained a sensitivity value of 45.5% for their first test and 78.8% for their second test. Collett et al. [41] uses an artificial intelligence program to compare their IRI images to an IRI image of a patient with breast cancer, while Sella et al. [39] used a mathematical algorithm to analyze the IRI data. Kandlikar et al. [42] reviewed some of these studies, as well as others that conducted research on thermography as a tool for breast cancer screening. From this review, the authors show that sensitivity of IRI varied based on testing and not on the year it was tested as shown in Table 1. Additionally, the authors discuss the ease of availability of new computational and modeling techniques that have yet to be fully explored and used with IR thermography. This shows and calls for more research on the topic, especially since advancements in technology have also advanced thermography. Table 2 shows the advancements in IR camera sensitivity, in terms of temperature readings, over the years.

Table 1: *Sensitivity of IR thermography of breast cancer screening at different years adapted from [42].*

Paper	Year	Sensitivity	95% CI
Keyserlink	1998	0.83	0.74-0.90
Wishart	2010	0.71	0.58-0.81
Wang	2010	0.79	0.73-0.84
Tang	2008	0.94	0.82-0.99
Parisky	2003	0.96	0.92-0.98
Kantos	2011	0.25	0.09-0.49
Button	2004	0.75	0.35-0.97
Arora	2004	0.9	0.79-0.96

Table 2: *IR camera thermal sensitivity progression adapted from [42].*

IR Camera	Year	Sensitivity (mK)
AGA 750	1972	230
ISI Videotherm	1980	150
Inframetrics 500M	1987	100
Inframetrics 600M	1995	50
Amber PM	2000	39
FLIR A8300	2005	20
FLIR SC 6000	2010	<20

Some of these works presented by Kandlikar et al. [42], as well as some of the previous work presented in section 2.1.1, used steady state thermography as their method of screening for breast cancer. Gonzalez-Hernandez et al. [43] reviewed the advancements, developments, and shortcomings of dynamic thermography in breast cancer detection. Dynamic thermography is an imaging technique that was established to reduce false negatives and positives of steady state thermography, described above. Unlike steady state thermography, in which acclimation of the breast is performed to reach a steady state temperature, dynamic thermography implements forced conduction or convection creating a cold stress on the breast. The authors discussed the need for further clinical studies the help decide which cold stress methods are best to be implemented on patients, as patients can feel discomfort from the cold stress. Also, the authors discussed the need of patient protocols prior to IRI and post-processing of the images, as well as better interpretation of these images.

According to Gonzalez-Hernandez et al. [43], one way to help find the best cold stress method to reduce patient discomfort is through numerical or theoretical analysis validated by experimentation on phantom models. The issue is obtaining appropriate breast models to conduct the numerical or theoretical analysis on, as each breast is anatomically different. Tackling the need to post-process

IRIs and the problem of interpreting these images, a computational approach is discussed by Gonzalez-Hernandez et al. [43]. Image processing techniques such as image registration allows for the dynamic thermograms to be prepared for other enhancements to the image. Implementing this with machine learning or artificial intelligence algorithms can help establish an autonomous process that can examine the thermograms. However, the criteria that would establish how to interpret the data would still be subjective if a well-established method is not created. The need to establish this method led to the numerical approach by first establishing a method to generate better breast models.

2.2 Thermal Modeling of Biological Systems

Biological systems are natural complex systems that are governed by the laws of nature. Thermal modeling is the process of creating an analytical model of a system using the fundamental laws of thermodynamics and heat transfer through experimentation. This modeling process can be implemented in biological systems as all living things are governed by these same laws. In this section, the analytic modeling of the human body will be explored through bioheat modeling, and the numerical techniques to further explore these models will be discussed.

2.2.1 Bioheat Modeling

In 1948, Bazett et al. [44, 45] explored the temperature of blood flow inside of a person as well as external parameters that affect the cooling of the system through invasive measurement tools. They concluded that the temperature in the limbs is not constant, or uniform, regardless of external conditions. These two papers, and many others like them such as Pennes [24], were the inspiration for finding noninvasive techniques to study internal body temperatures, or bioheat phenomena. Pennes' bioheat equation is the following:

$$\rho_t c_t \left(\frac{\partial T_t}{\partial t}\right) = \nabla \cdot (k_t \nabla T_t) + \rho_b c_b \omega_b (T_a - T_t) + q_m \quad (1)$$

where ρ is density, c is the specific heat, T is temperature, t is time, k is the thermal conductivity, ω_b is the blood perfusion rate, and q_m is the metabolic heat generation rate, while the subscripts t, b and a stand for tissue, blood, and artery respectively. In 1997, Xuan and Roetzel [46] proposed an alternative porous-media heat transfer model to the continuum bioheat transfer models developed by Pennes [24], which models the effect of blood flow on tissue temperature and was later modified by others such as Charny [47]. Later on, Nakayama, Kuwahara, and Lui [48] further improved on the porous-media bioheat heat transfer equations by developing three-energy equation models for a multi-dimensional and anisotropic model for countercurrent heat transfer phenomena in the blood circulatory system. Mahjoob and Vafai [49] later developed a more complex model with analytical solutions for dual layer biological media in relation to porous-media theory. Wang and Fan [50] conducted a study on both the continuum, or mixture theory, and porous-media bioheat transfer models to identify their characteristics and discuss fundamental theories based on their involvement with a macroscopic model. They concluded that both models take advantage of simplicity, but do not offer connections between microscale and macroscale properties, as well as they do not "accurately describe the rich blood-tissue interaction" [50], although the porous-media has recently overcome these issues, which points in the direction of developing a closure theory for these equations.

2.2.2 Numerical Simulations

In 2017, He and Liu [51] developed their coupled continuum-discrete (CCD) model and compared it to previously used bioheat models, such as Pennes [24], Nakayama, Kuwahara, and Lui [48], as well as others, numerically. They used a finite element method as well as a parallel alternating

direction explicit finite difference method, which they developed in one of their previous papers [52], to compare the analytic solutions of the previous models and CCD on a well-known geometry of a “2D tissue immersed with a single vessel” [51]. They were also able to validate the performance of CCD on a realistic liver model domain reconstructed from MRI data to evaluate the vascular network thermal effect of a liver with a tumor as a heat source. He and Lui [51] showed a comparison of the liver temperature distribution analytic solution of Pennes [24] model and the numerical solution of the CCD model in their paper.

IR thermography has been a useful tool in various fields of study, but its usefulness in numerical simulations have been underutilized. Kakutaet al. [53] performed a comparison study of IRI of skin surface temperature under various thermal conditions. In their study, they conducted a numerical simulation bioheat model on a simplified geometric 16-cylinder-segement model of the human body under specific conditions. Then, they gathered IRI images of different parts of the human body, such as the limbs, under the same conditions as the bioheat model to help establish a calibration offset. Lastly, they tried to recreate IRIs at different conditions using the bioheat model offset. A flowchart of the entire process is shown in Fig. 3. They concluded that the comparison between the original and recreated IRI “is effective in eliminating the influence of the thermal environmental conditions” but the difference between them varies depending on the segment. This study utilized IR thermography and bioheat numerical modeling as tools to conduct noninvasive research. This comes to show the potential of bioheat numerical simulations and their application to the biomedical field with the use of image processing to build the modeling domains, as well as the use of IR thermography as a tool to create physical constraints and conditions for these models.

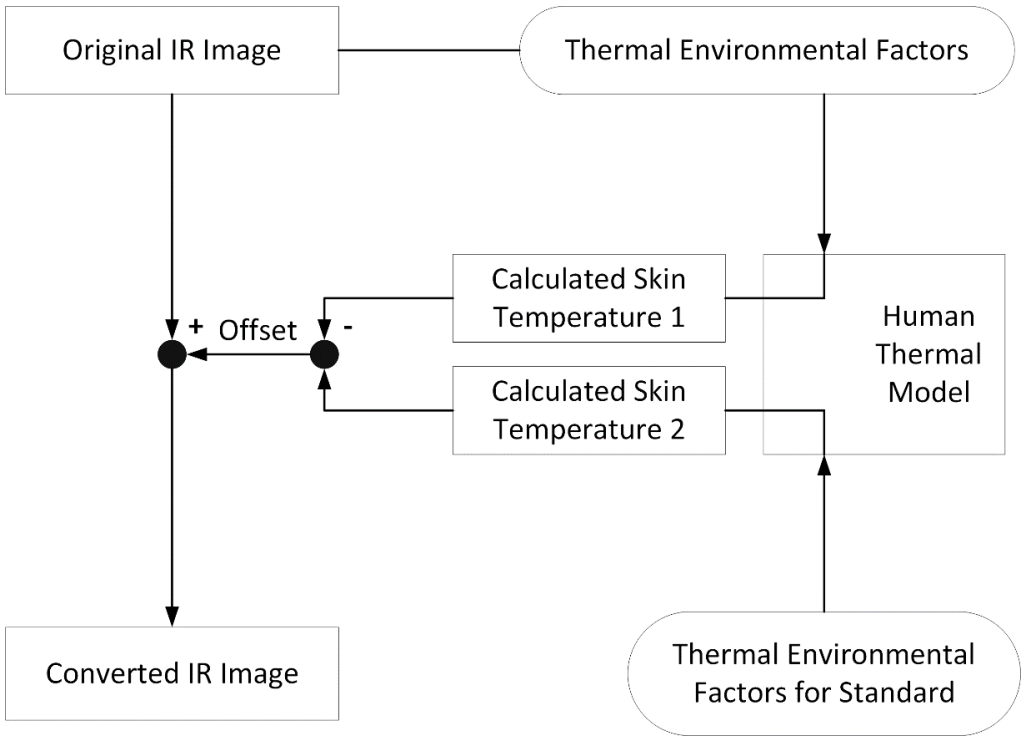

Figure 3: *Process of converting an IR image from one environmental condition to an IR image at a different condition using bioheat modeling of a person; redrawn from [53].*

2.4 Image Processing

Image processing, or digital image processing, is a computational technique that implements computer algorithms to process, or modify, a digital image depending on the user need. Computer graphics is another computational technique that generates some sort of digital image or geometry using specific computer algorithms. Although these techniques were developed and are mostly used in computer science, their usability has been tested for many applications in different fields of study. In this section, the image processing techniques, image registration and reconstruction, will be discussed as well as their applications in the medical and thermography fields.

2.4.1 Image Registration and Reconstruction

Image registration is the process of aligning two or more images by having one image as the target image and geometrically transforming or converting the other images to match the target image.

The advancements and developments of IRI technology were motivated by the military due to a need for better detection and recognition systems. In 1996, Kaltenbacher and Hardie [54] developed an algorithm to reconstruct high-resolution images from IRI utilizing how the detector arrays of IR cameras scan images, as well as reviewed the limitations and theory of these registration and reconstruction algorithms. Their algorithm uses a digital signal processing method called uncontrolled microscanning, which is "the process where the shifts for each recorded frame are unknown and must be estimated before forming an estimate of the high resolution image" [54]. This is done with the use of an image registration method called the gradient method, Eq. 2,

$$f(m,n) \cong f(m_0,n_0) + (m-m_0)\frac{\partial f(m_0,n_0)}{\partial m} + (n-n_0)\frac{\partial f(m_0,n_0)}{\partial n} \tag{2}$$

which uses a given function's Taylor series expansion. In this equation, m and n are discrete variables that represent the x and y directions, respectively. The terms $(m-m_0)$ and $(n-n_0)$, which are relabeled as S_x and S_y, represent the shifts in the x and y directions, respectively, that are needed to be solved before reconstructing the image. The authors used the least square method, Eq. 3, to solve for S_x and S_y for sample points $M$and N in the x and y direction, respectively.

$$\frac{1}{MN}\sum_{m}^{M}\sum_{n}^{N}\left[f(m,n) - f(m_0,n_0) - S_x\frac{\partial f(m_0,n_0)}{\partial m} - S_y\frac{\partial f(m_0,n_0)}{\partial n}\right]^2 \tag{3}$$

The authors then expanded this equation, set the first derivatives to zero, wrote them in matrix form and solved for the shifts as shown in the equation below, full derivation in [54]:

$$S = M^{-1}\cdot V \tag{4}$$

After solving for the shifts, they can be used to reconstruct the image by finding a set of aliased spectra that were summed up to estimate an alias of free spectrum with the use of multiple input signals. This can be done with the use of a Fourier transform, Eq. 5, due to its shift properties

$$F_k(u,v) = e^{j2\pi(\delta_{kx}u+\delta_{ky}v)}F(u,v) \tag{5}$$

where F is the Fourier transform, u and v are the frequency variables, with corresponding shifts δ_{kx} and δ_{ky}, in the x and y directions, and the subscript k is the signal number. Since the domain for the data set is discrete and not continuous, this continuous Fourier transform (CFT) can be turned in a discrete Fourier transform (DFT) with the use of sampling and can be further simplified using the two parameters L_x and L_y, "which [represent] the desired increase in resolution from the original data to the final reconstructed data" [54] in the x and y directions, respectively. Further derivation and theory are shown in [54]. The DFT is given by the following equation, Eq. 6:

$$F_k(m,n) = \frac{1}{T_x T_y}\sum_{b=-L_x}^{L_x-1}\sum_{g=-L_y}^{L_y-1} F\left(\frac{2\pi m}{MT_x} + b\omega_x, \frac{2\pi n}{NT_y} + g\omega_y\right) \tag{6}$$

for $m = 0, 1, \ldots M-1$ and $n = 0, 1, \ldots N-1$, where M and N are the sample size, T_x and T_y are the sampling periods, and ω_x and ω_y are the corresponding sampling frequencies in the x and y directions, respectively. Eq. 6 can be rewritten in a generalized matrix form, which can be used to solve for $F_{m,n}$, the "samples of the alias free CFT of the high resolution signal" [54] with the following equation, Eq. 7:

$$F_{m,n} = \phi_{m,n}^{-1} G_{m,n} \tag{7}$$

where $G_{m,n}$ are the values of the DFT of each signal at the discrete frequency points, m and n, and $\phi_{m,n}$ are the phase shift information at m and n. Eq. 7 works well for an ideal case where the total

number of input images is $4L_xL_y$, but for a bigger input image number the method of least square can be used which results in the following equation, Eq. 8:

$$F_{m,n} = (\phi^T\phi)^{-1}\phi^T G_{m,n} \tag{8}$$

Once the alias free spectrum has been solved and inverse Fourier transform is done on the data to obtain the high-resolution image. The entire reconstruction process is shown in Fig. 4.

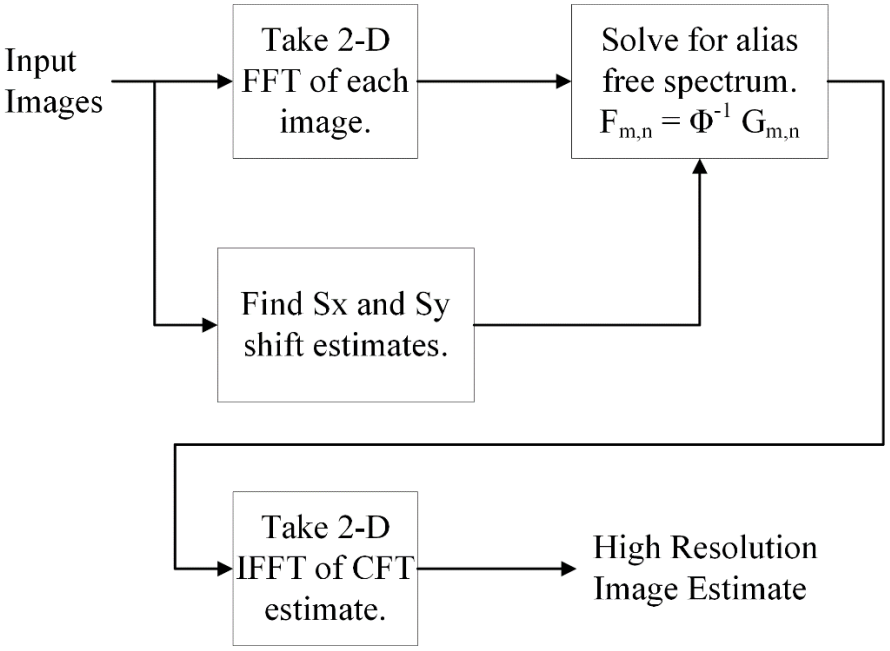

Figure 4: *Schematic of the reconstruction process of high-resolution images; redrawn from Kaltenbacher and Hardie [54].*

In 2000, Alam et al. [55] developed their own high-resolution reconstruction with the use of forward looking IR detector arrays and the uncontrolled microscanning method for practical scenarios such as "an imager is mounted on a moving and/or vibrating platform, such as an aircraft" [55]. Alam et al. [55] create a high-resolution pixel grid which helps enhance the low-resolution pixels using their detector properties. After this, they begin the image registration process of solving for the shifts for the low-resolution image frames in the same way as Kaltenbacher and Hardie [54] solved for image shifts. These shifts were then placed on the high-

resolution frame grid at 1/L intervals from the reference frame, where L is the microscan level. Anywhere in the high-resolution grid which does not have a corresponding low-resolution frame was filled in using the weighted nearest neighbor method. To minimize the mean square error between the input image and the desired high-resolution reconstruction image, a linear filter called the Wiener filter is used after the weighted nearest neighbor method.

Kaltenbacher and Hardie [54], and Alam et al. [55] took advantage of how IR detector arrays scan and create the pixels for the image output to use the uncontrolled microscanning method to reconstruct a higher-resolution image, but the algorithm created by Alam et al. [55] was faster and more practical for real-time applications compared to Kaltenbacher and Hardie [54] due to how the authors utilized their specific detector array in their algorithm as well as the use of the Wiener filter. Figure 5 shows a comparison of both algorithms used on an IR image of vehicles taken by an aircraft.

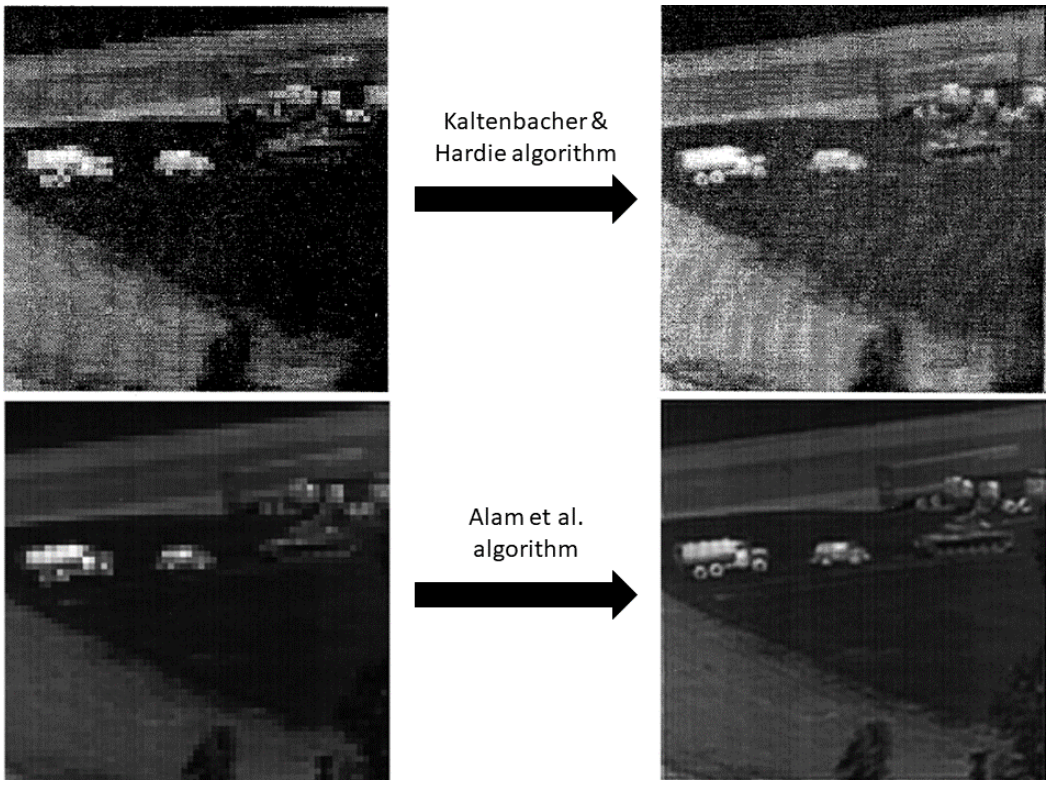

Figure 5: *The top row shows the original IRI reconstructed under Kaltenbacher and Hardie [54] © 1996, IEEE reconstruction algorithm to give a high-resolution image. The bottom row shows Alam et al. [55] © 2000, IEEE reconstruction algorithm on a similar image resulting in an even better high-resolution image.*

2.4.2 Medical Applications of Image Processing

Medical imaging has advanced over the years due to technological advancements and image reconstruction methods. One of these advancements was the computerized tomography (CT) scanner, an imaging technique which obtains multiple X-ray images at different angles and "uses computer processing to create cross-sectional images (slices) of the bones, blood vessels and soft tissues inside your body" [56]. In 1983, Medoff et al. [57] created a method that enhanced the image reconstruction process of CT scans of an object when encountering limited-data problems, but with some prior information of the object. In 1987, Reeds and Shepp [58] approached the problem of limited-angle reconstruction of CT scans based on previous work done by Medoff et al. [57] and others. The authors did this by creating a computationally efficient algorithm based on mathematical models they developed for this problem. In 2010, Jin et al. [59], took on their own

approach to solve the limited-angle reconstruction problem by focusing on the optimization of their previous algorithm called the total variance regulation algorithm. Chen et al. [60] further extended this work to show results based on their study and opened the floor for further enhancements.

Another advancement was the positron emission tomography (PET) scan, which is taken by injecting a patient with small radioactive materials who is then scanned and imaged using "a special camera and a computer to evaluate organ and tissue functions" [61]. In 1987, Rogers, Harrop, and Kinahan [62] reviewed papers on three-dimensional image reconstruction of PET images, some of which were an extension of two-dimensional image reconstruction. They suggested their own algorithms and techniques to extend and enhance these previous works. Kinahan and Rogers [63] presented their suggested work with validated results on generalized simulated projection data, which opened the door for improvements and further applications. Defrise, Townsend, and Clack [64] clarified and explored different algorithms, such as Kinahan and Rogers [63], in order to create generalized guidelines that helped establish which appropriate techniques to use for specific types of problems based on properties and characteristics that they created.

2.5 Conclusions from Literature Review

Due to the technological advancements of IR cameras, IR thermography is receiving attention in recent research works on breast cancer detection. Previous work has validated the use of IR thermography as an adjunctive breast cancer screening modality through numerical simulations and image processing techniques. IR thermography as a screening method is safer and noninvasive compared to most common screening modalities. Also, studies of the bioheat equations, with the use of numerical simulation schemes, show great promise in the field of cancer detection and

thermopathology. Although a computerized IRI program has been created for the detection and localization of tumors in breasts, there is a need for more studies to establish the effects of thermal parameters of the tumor and surrounding tissue on the detection capabilities of this program.

3 Objective

The literature review shows that there is potential for the use of IR thermography as a method to detect breast cancer. Recent advancements in IR and computational technology indicate that this technique needs to be further evaluated as an adjunctive screening modality. The computerized IRI program developed at RIT [20, 21, 23, 27] is able to detect and localize breast tumors and it has been validated with seven biopsy-proven cases. In their work, the thermal properties were derived from the literature. This work focuses on understanding the effect of breast and tumor properties on the detection ability. In this work, a parametric study of the thermal parameters used in the computerized IRI program, specifically the tissue thermal conductivity and blood perfusion rate, will be conducted using numerical simulations and image processing. The main objectives of this work are the following:

1. Study the effects of tissue thermal conductivity and blood perfusion rates in tumor and in the breast tissue surrounding the tumor on the heat transfer and comparison with the clinical IRI images
2. Obtain optimum combinations of properties that yield the best match between the simulated thermal images and the clinical IRI images
3. Form a basis for selecting thermal properties based on the thermopathology of breast cancers
4. Extend the use of IR thermography as a tool for cancer research

4 Methodology

The method employed in this work is an extension of the algorithm developed by Gonzalez-Hernandez et al. [22, 23] and Recinella et al. [27]. Therefore, some of the processes implemented in these previous studies were learned, recreated, and utilized as a baseline for the parametric study. However, refinements were needed to improve the functionality of the program. A parametric study related to the effect of the tissue thermal conductivity and blood perfusion rate on the accuracy of thermal prediction was conducted. As these properties were varied, the resulting thermal images from the program were compared with the IRI images. The agreement was compared using normalized root mean square error. Image registration between the computed images and the IRI images were necessary and an algorithm was developed to meet this need. These techniques are discussed in this chapter.

4.1 Detection and Localization of Breast Tumors

This work is a continued collaboration between Rochester Institute of Technology and Rochester General Hospital (RGH). In a previous study, a method to detect and localize a tumor of biopsy-proven breast cancer patients using IRI images was developed [20, 21, 23, 27]. The process can be broken down into five steps: i) clinical setup and image acquisition, ii) generation of a patient-specific digital breast model, iii) conducting numerical simulations, iv) image processing, and v) inverse heat transfer modeling to determine size and location of the tumor. Steps 1 to 4 will be discussed in this section; however, step 4 will be further discussed in section 4.3. Step 5 will be briefly discussed in sections 4.2 and 4.4 as this work will not utilize the inverse heat transfer approach as a fixed tumor diameter and location will be used from the prior study.

4.1.1 Clinical Setup and Image Acquisition

This study begins with the collection of medical information and IRI images of 30 women with biopsy-proven breast cancer recruited as described by Recinella et al. [27]. This was done through an approved Institutional Review Board protocol at RGH with all personnel who worked on this project undergoing human subjects training and completing a Collaborative Institutional Training Initiative certification. Prior to imaging, a consent form was filled out by each patient so that they may participate in this study. All patient personal identification was removed during the imaging process. The IRI images were then captured using a rotating infrared camera setup with a screening table setup illustrated in Fig. 6. The camera is a FLIR SC6700 infrared camera with a resolution of 640×512 pixels and a thermal sensitivity of 0.02 ºC. Eight equidistant images were captured at an upwards tilt of 25º from the vertical, as shown in Fig. 7a. Prior to capture, the patients laid in prone position and were acclimated to reach a steady-state condition. An example of captured multiview IRI images is shown in Fig. 7b. For more details on the clinical setup and image acquisition refer to Recinella et al. [27].

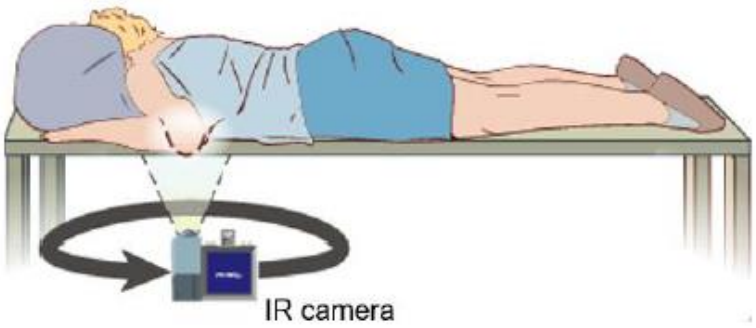

Figure 6: *Medical illustration of screening table setup conducted by Recinella et al. [27], reproduced from [21] with permission.*

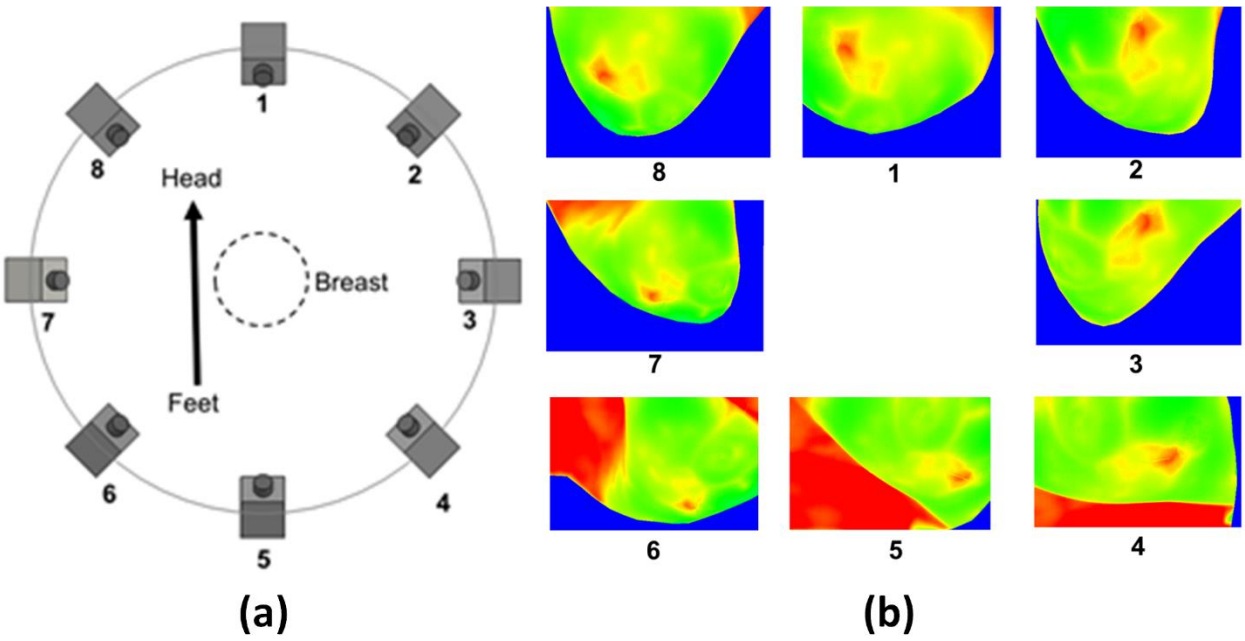

Figure 7: *Illustration of IR camera setup (a) and corresponding captured IRI images (b) at eight equidistant positions, adapted and reproduced from [21] with permission.*

4.1.2 Digital Breast Models

In a previous study, Gonzalez-Hernandez et al. [22] developed a method to generate patient-specific digital breast models using MRI images captured at RGH. The patient-specific digital breast model is a 3D model of the breasts reconstructed from MRI images using image processing and computer graphics techniques. The process begins with importing the sequential MRI image slices into the ImageJ software where edge detection was done on all images to outline the breast. Then, to reduce noise due to the capture of other parts in the MRI, segmentation was implemented to highlight the breast so the focus can be on the outline features. Once this was done on all slices, the segmented images were stacked to generate a volumetric rendering of the breast using the Marching Cubes algorithm. The 3D object was then imported into the Meshmixer software where the object was smoothed using the software's average mesh angle algorithm. Finally, the new geometry went through one more refinement in Autodesk Recap Photo before being used for

numerical simulations. The process is seen in Fig. 8 and more details of the process are found in Gonzalez-Hernandez et al. [22].

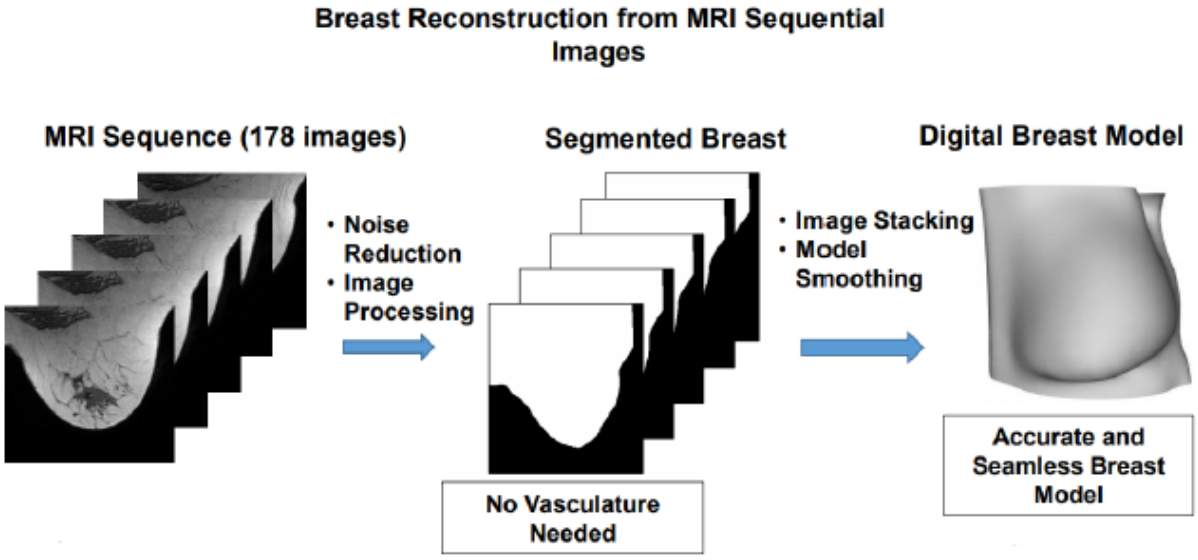

Figure 8: *Process for generating patient-specific digital breast models from MRI, reproduced from [21] with permission.*

4.1.3 Numerical Simulation

Once the digital breast model is created, numerical simulations can be implemented using Pennes' bioheat equation [24], Gautherie's model for tumor metabolic activity [25, 26], and ANSYS Fluent. Before any numerical simulations are done on the model, mesh refinement is performed on the computational domain to improve accuracy. A uniform mesh is used throughout the model, with the surface, location F in Fig. 11, having a finer mesh to accurately compute temperature gradients [22]. A steady-state Pennes' bioheat equation is implemented into Fluent by adding a convective source term due to blood flow and a heat generation source term due to metabolic activity. This was done through a User-Defined Function (UDF), an external code written in C++ that gives ANSYS Fluent custom commands based on what the user may need. These terms differ depending on whether the tissue region of the breast is considered healthy or unhealthy due to the

tumor. For the unhealthy region, a higher perfusion rate (ω) is implemented, and the metabolic activity is taken from Gautherie's model, which is dependent on the tumor diameter (d_t). Pennes' bioheat equation can then be split into the following:

$$\nabla \cdot (k_h \nabla T) + \rho_b c_b \omega_h (T_a - T) + Q_h = 0 \tag{9}$$

$$\nabla \cdot (k_t \nabla T) + \rho_b c_b \omega_t (T_a - T) + Q_t = 0 \tag{10}$$

where the subscripts h and t stand for healthy and tumorous, respectively, and

$$Q_t = \frac{3.27 \times 10^6}{468.5\, ln(100 d_t) + 50} \tag{11}$$

For equations 9 and 10, $k_h = k_t = k$ due to the thermal conductivity being modeled as constant throughout the breast regardless if the tissue is healthy or cancerous. This was done due to the inverse heat transfer iterative algorithm that was used to find an estimate to this value [23].

Once the governing equations are set up, the following boundary conditions are implemented on the model, Fig. 9:

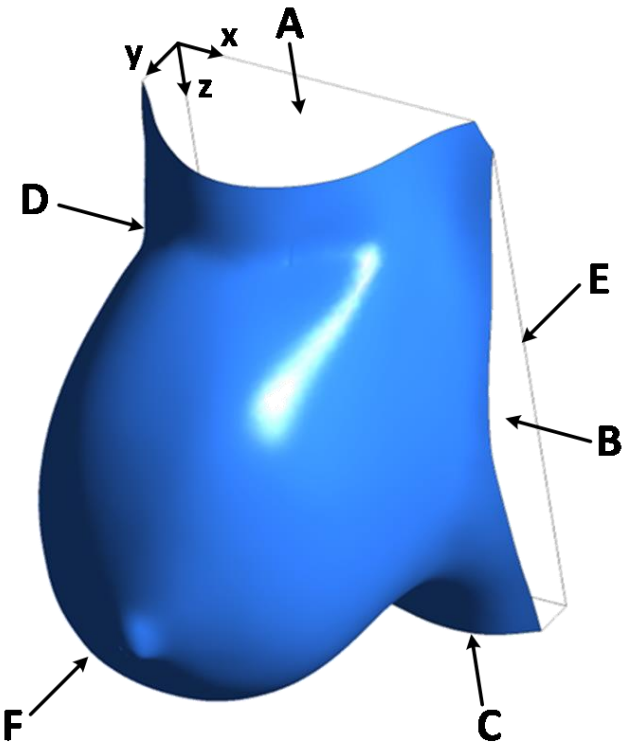

Figure 9: *Digital breast model with top, right side, bottom, and left side labeled as (A-D), respectively, and F and E are the breast surface and chest wall, respectively.*

$$\left.\frac{\partial T}{\partial \boldsymbol{n}}\right|_{A,B,C,D} = 0$$

$$T_E = T_c$$

$$-k\left.\frac{\partial T}{\partial \boldsymbol{n}}\right|_F = h(T - T_\infty)|_F$$

where $\boldsymbol{n}$ represents the normal vector at the corresponding location, T_c is the core body temperature, h is the heat transfer coefficient, and T_∞ is the ambient temperature. These boundary conditions imply that heat is transferred due to conduction from the chest, location E in Fig. 9, into the breast and heat is removed due to conduction at the breast surface, location F in Fig. 9, without any heat loss at the sides, locations A-D in Fig. 9. The thermophysical properties and parameters that were used for this study are shown in Table 3 and 4, respectively.

Table 3: *Thermophysical properties table for the digital breast model adapted from [22, 23, 27].*

Property	Value	Unit
Perfusion rate of healthy tissue (ω_h)	1.8×10^{-4}	s^{-1}
Perfusion rate of tumor (ω_t)	9×10^{-3}	s^{-1}
Metabolic activity of healthy tissue (Q_h)	450	W m^{-3}
Temperature of arteries (T_a)	37	°C
Specific heat of blood (c_b)	3,840	J kg^{-1} K^{-1}
Density of blood (ρ_b)	1,060	Kg m^{-3}
Core temperature (T_c)	37	°C
Ambient temperature (T_∞)	21	°C
Heat transfer coefficient (h)	13.5	W m^{-2} K^{-1}

Table 4: *Parameter range values for the tissue thermal conductivity of the breast and breast tumor size and location adapted from [23].*

Parameter	Minimum value	Maximum Value	Units
k	0.15	2	W $m^{-1}K^{-1}$
d_t	0.0099	0.07	m
x_t	x_{min}	x_{max}	m
y_t	y_{min}	y_{max}	m
z_t	z_{min}	z_{max}	m

The range of values in Table 4 all depend on how fatty or dense the breast is, Gautherie's model for metabolic activity, and computational domain of the digital breast model, Fig. 10. These values were stored in the UDF in which Fluent read and implemented them into the simulation. Before running the numerical simulation, a convergence criterion for the residuals was selected to be 1×10^{-16}. This criterion not only allows for a more accurate model but helps eliminate discrepancies between the healthy and unhealthy regions which map to each other to solve equations 8 and 9 simultaneously. Once everything was set up, Fluent obtained the numerical solution to these equations which generated computed temperature images as shown in Fig. 11. This technique was validated on seven subjects, as discussed in Gonzalez-Hernandez et al. [23], and therefore one of these subjects has been selected for this study.

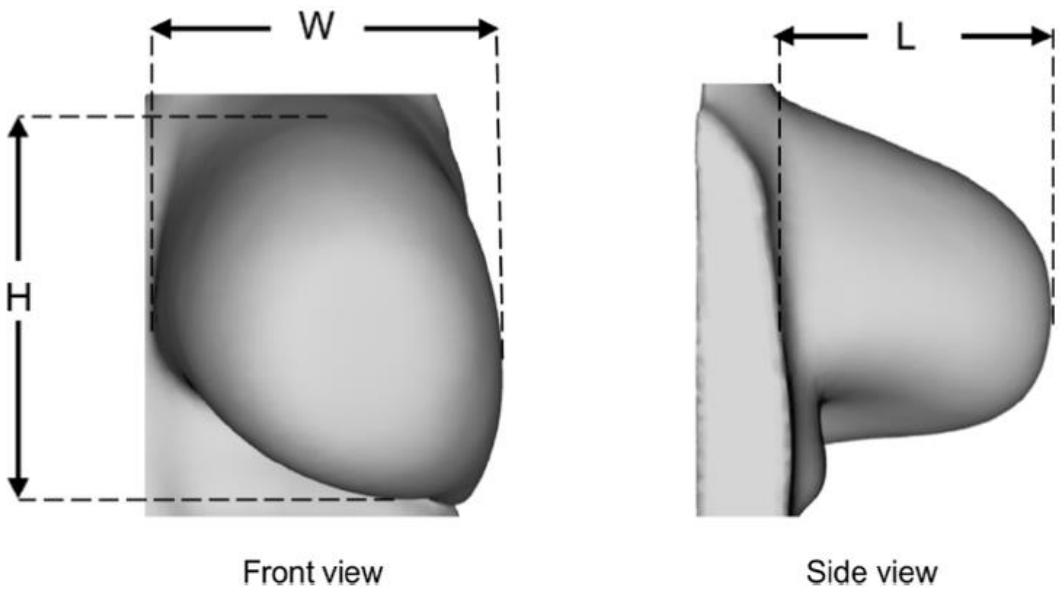

Figure 10: *Front and side views of computational domain of patient-specific digital breast model; adapted reproduced from [21] with permission.*

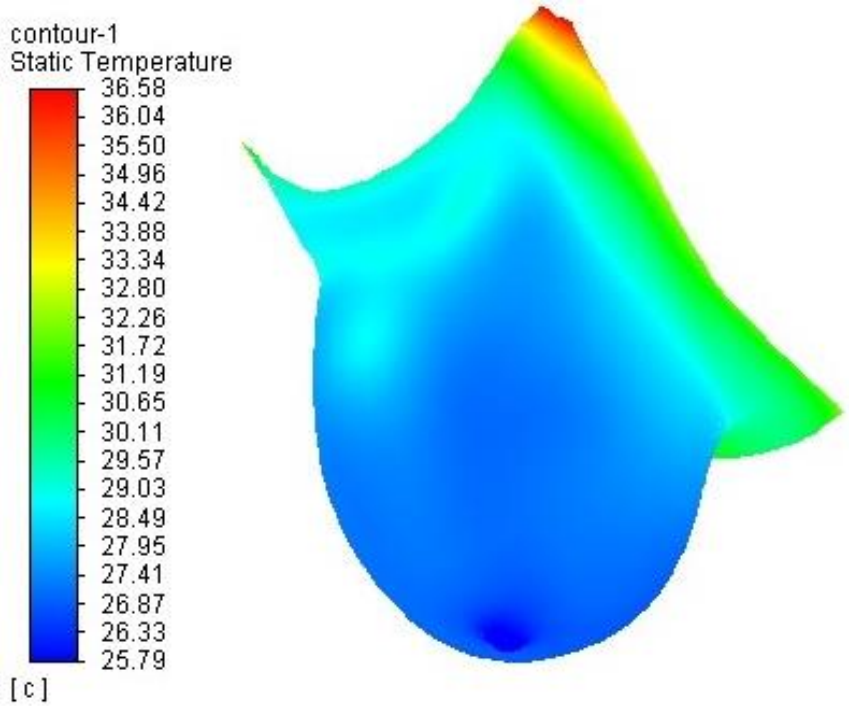

Figure 11: *Example of a computed temperature image simulated from ANSYS Fluent.*

4.2 Parametrization in the Present Study

The previous study utilized the multiview IRI and computed temperature images with an iterative algorithm to detect and localize a tumor in biopsy-proven breast cancer patients. This was done through an inverse heat transfer approach by parameterizing the thermal conductivity (k), tumor diameter (d_t), and tumor position (x_t, y_t, z_t). These parameters were initially set to values in the range shown in Table 4 through an external text file, which gave an initial computed temperature image that was then compared to the corresponding IRI image. Once the temperature values were compared, new parameter values were obtained through inverse heat transfer, overwriting the previous text file which was fed to the UDF. This allowed for the simulation to be run again so that new computed temperature images were generated. This was done iteratively until a convergence criterion was reached which then gave the best estimated parameters.

For this work, the thermal parameters are chosen for conducting the parametric study as these essentially govern the heat transfer process within the breast. These thermal parameters are (i) tissue thermal conductivity (k), (ii) blood perfusion rate of the tumor, ω_t and (iii) blood perfusion rate for the surrounding breast tissue, ω_h. The ranges of these parameters are derived from the respective ranges suggested by Gautherie [25, 26]. In this section, the method for parameterization of these thermal parameters and the values of these parameters will be discussed.

4.2.1 Modified Numerical Simulation

To parametrize the three thermal parameters, k_t, ω_t and ω_h, a modification to the UDF and numerical simulation is needed. In the UDF, the values shown in Table 3, and the source terms from equations 8 and 9 are implemented as well as the tumor diameter and position taken from patient placement and pathology data discussed in section 4.1. Also, since the diameter of the tumor is known, Gautherie's metabolic activity model, equation 11, is implemented to determine

the heat generation rate. This time the three thermal parameters are written in an external text file and will be varied. The parametric study is divided into two cases:

Case 1: consisting of varying the blood perfusion rate of the tumor while holding the blood perfusion rate of the breast tissue constant, and

Case 2: with varying the blood perfusion rate of the breast tissue while holding the blood perfusion rate of the tumor constant.

For each of these cases, the thermal conductivity value is systematically varied in the range indicated by Gautherie to generate the parametric plots. The numerical simulation and boundary conditions are the same as the ones indicated in section 4.1. This will be further discussed and explained in section 4.3.

4.2.2 Thermopathology

The thermal parameter values used in the parametric study are based on the work reported by Gautherie [25, 26]. In his findings, Gautherie reported the values for the effective tissue thermal conductivity of the breast at different breast densities. The effective tissue thermal conductivity is dependent on the tissue density, meaning that the denser the tissue, the more conductive it is. Gautherie also reported the blood perfusion rate of a healthy tissue type and one that has been affected by a carcinoma, which are 1.8×10^{-4} 1/s and 9×10^{-3} 1/s, respectively. From these values it can be observed that tissues with a carcinoma have a higher blood perfusion rate making them more vascular.

4.3 Image Processing

Image processing has been a useful and crucial tool in the previous study as it was used to generate the digital breast model and to conduct the inverse heat transfer approach. To implement the inverse heat transfer approach, the computed temperature images had to be aligned with the corresponding IRI image. In the previous study, the model was manually rotated and translated in Fluent to match the computed temperature image to the IRI image and the type of movement with coordinates were saved to an external text file. Then, with image registration the images were better aligned to increase accuracy and comparison for the inverse heat transfer approach. In the present work, these external text files were utilized in the modified simulation so that the computed temperature images can be obtained. Image registration is also used with some modifications to account for the change in temperature ranges, which will be discussed in this section. Also, the ROI and other image processing techniques associated with it that are used in the present work will be discussed in this section.

4.3.1 Image Registration

As described in section 2.4, image registration is the process of aligning two or more images by having one image as the target image and geometrically transforming or converting the other images to match the target image. The target image is also known as the fixed image while the images that are being aligned, or registered, are known as the moving images. In this study, an automated intensity-based multimodal affine image registration is used on the IRI image (fixed image) and the computed temperature images (moving images) through MATLAB's Image Processing Toolbox.

Prior to image registration, the images had to be pre-processed to ensure that the focus is on the breast outlines and image pixel intensity patterns of the breast interior are clearly registered. The pre-processing steps are: i) manually cropping the fixed and moving images and ii) converting the images into grayscale images. For step 1, this is done in MATLAB by loading up the image and manually selecting the region by dragging the mouse around that region. This will give a vector that gives a rectangular metric, [xmin, ymin, width, height] where xmin and ymin are the left lower corner x- and y-coordinates, and width and height are the width and height of the rectangle in pixels. This rectangle is then used with the MATLAB function *imcrop()* to crop the fixed and moving images. Once these images are cropped, they are transformed into grayscale images using MATLAB's *rgb2gray()* function. The image selection and registration processes are done manually, but automatic registration is recommended in the future work.

After pre-processing, the optimizer and metric for the image registration had to be configured so that the image registration is multimodal, which is done through MATLAB's *imregconfig()* function. Once the configuration is done, the grayscale moving images can be registered to the grayscale fixed images using MATLAB's intensity-based automatic image registration function *imregister()* and an affine transformation. The affine transformation allows the moving image to translate, rotate, scale, and shear so that it matches the fixed images. This is the best fit as the digital breast models created from the MRI images were captured differently than the IRI images of the same breasts. A flow chart of the image registration process is shown in Fig. 12.

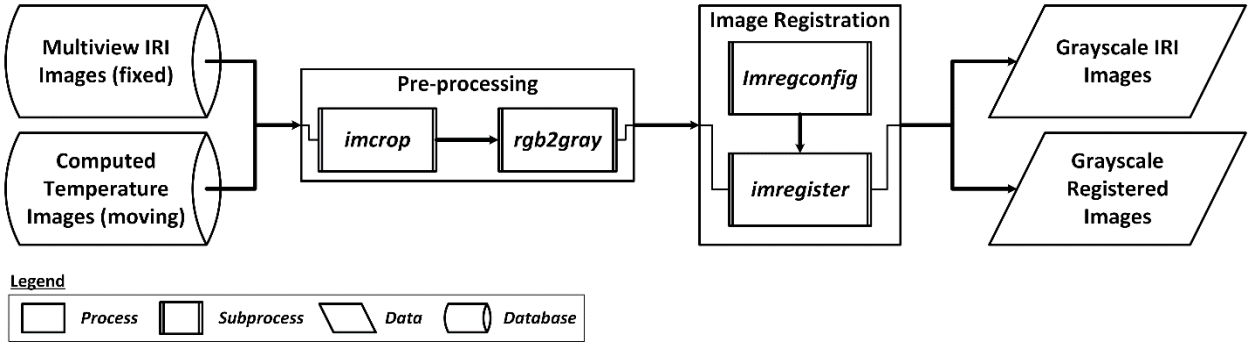

Figure 12: *Image registration process of the Multiview IRI and computed temperature images.*

4.3.2 Region of Interest

After the computed temperature images are registered to the IRI image, a region of interest (ROI) needs to be selected. In the previous study, the ROI is a region in the breast that has a hotspot or some sort of gradual temperature difference. The ROI will be the same as the previous study but in the case of no hotspot regions, a region with an obvious color distinction will be chosen. An example of an ROI is shown in Fig. 13. Similar to cropping the image for pre-processing, a rectangular metric vector will be manually obtained from the ROI in the grayscale IRI image and will be used to crop the grayscale registered computed temperature images.

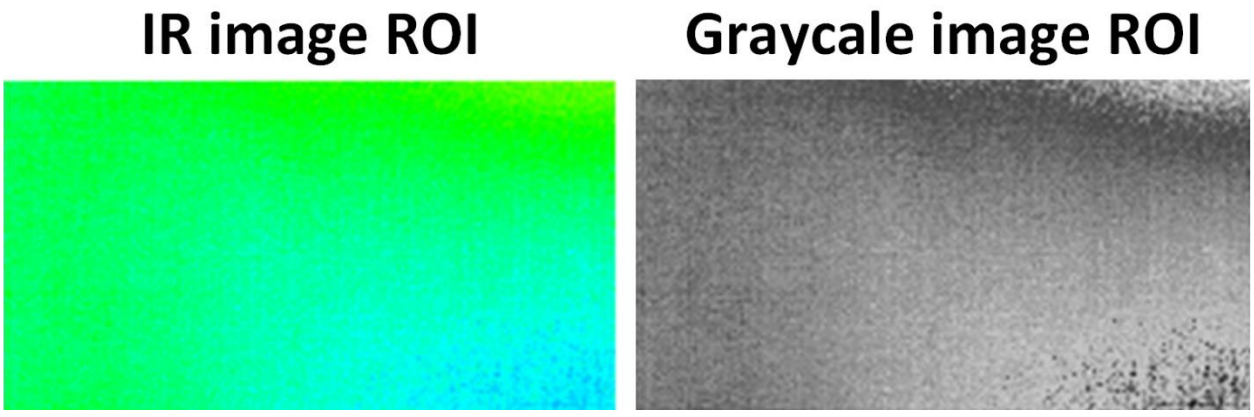

Figure 13: *Example of a ROI from the IRI image (left) and corresponding grayscale image (right) selected based on clear distinction in color due to temperature difference.*

4.4 Thermal Comparison

To conduct the parametric study, a quantitative comparison is needed between the simulated thermal images and the IRI images. Although the images themselves can be compared to the difference in color at the ROI qualitatively, a method needs to be implemented to convert these colors to quantitative data. Since the color changes in these images are due to temperature changes, a conversion into temperature data will be implemented. Once these images are converted into temperature data, the temperature difference between the IRI and computed temperature images can be obtained for comparison. The methods to convert these images into temperature data and to obtain the thermal comparison are discussed in this section.

4.4.1 Assigning Temperature Values

Once all images are cropped using the ROI, temperature values can be assigned to each image. This is done by converting the data type of the image into temperature data similar to what was done for the inverse heat transfer approach discussed in Gonzalez-Hernandez et al. [23]. The data type of a grayscale image is either an 8-bit or 16-bit unsigned integer matrix with the size depending on the pixel count. For example, if the pixel count is $n \times m$, then the matrix size will also be $n \times m$. Since the grayscale computed temperature images were registered, their pixel count is the same as the grayscale IRI images which means that the cropped ROI images' pixel count will all be the same. The data type of the images and the minimum and maximum known temperature values of the ROI governs the transformation into temperature data through a conversion factor. The conversion factor is based on the color or intensity level of the image which for grayscale can be from $2^8 - 1$ for 8-bit and $2^{16} - 1$ for 16-bit. In the images, the values from 0 to the conversion factor indicate how many shades of the grayscale coloring there are. This means

that 0 will be white, the last number is black, and the numbers in between are different shades of gray.

The transformation begins with the image being converted from its unsigned integer matrix into a double-precision matrix using the MATLAB's Image Processing function *im2double()*. Then, this double-precision matrix is multiplied with the conversion factor to assign an intensity value to each pixel. The minimum and maximum values of these intensity values are then obtained and stored. Once this is done, the temperature values are assigned and bounded onto the matrix through a linear interpolation equation:

$$T_{i,j} = T_{min} + \frac{T_{max} - T_{min}}{I_{max} - I_{min}} (I_{i,j} - I_{min}) \tag{11}$$

where $T_{i,j}$ is the temperature at the pixel index (i,j), T_{min} and T_{max} are the known minimum and maximum temperature values at the ROI, respectively, I_{min} and I_{max} are the minimum and maximum intensity values of the ROI image, respectively, and $I_{i,j}$ is the intensity value at the pixel index (i,j). This formula assures that the temperature values are bounded in between the minimum and maximum known temperature values in the ROI. To obtain the minimum and maximum temperature values of the IRI images, the ROI is manually applied to these images in the ThermoVision ExaminIR software. In this software, these values are obtained manually or through the statistical function built into the software. To obtain the minimum and maximum values for the computed temperature images, the ROI is estimated based on the contours seen in the registered ROI image and a probe is manually implemented, as shown in Fig. 14.

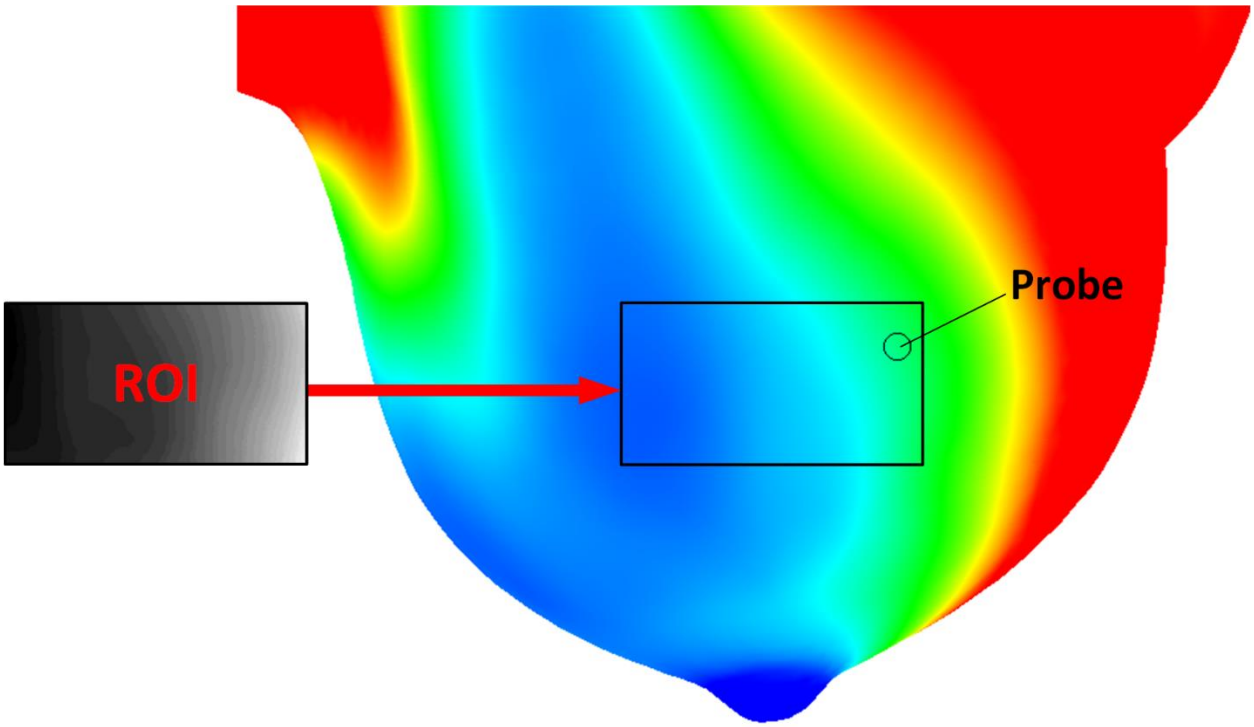

Figure 14: *Example of estimating ROI a computed temperature image using the contour pattern of registered ROI image with probe used to obtain minimum and maximum temperature values.*

After converting the ROI images into temperature data, filtering is done on the data to smoothen out any noise variations between values created from the conversion. An averaging, or mean, filtering approach is used on the data by getting a 3×3 subset of the data, taking average of the temperature values in that grid, and putting those averaged values into a new reduced matrix of size $N \times M$. An illustration of this method is shown in Fig. 15. The issue that arises from this filtering method is based on the size of the temperature data matrix, which may skew or allow for uneven filtering. Depending on the matrix size, the edges of the data may not be properly filtered. This can be avoided by adding an additional row or column along an edge or edges with a value of 0ºC, also known as zero-padding.

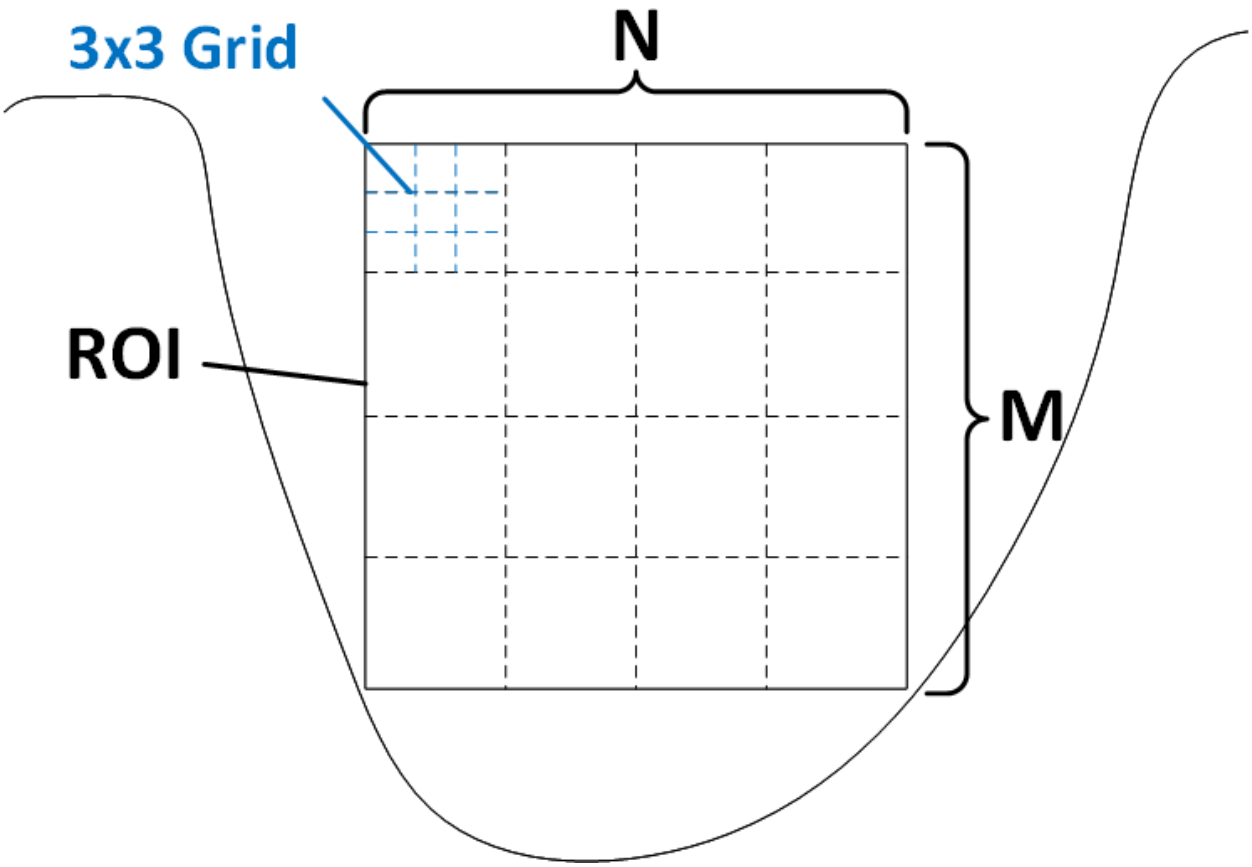

Figure 15: *Illustration of filtering technique used in the present work*

4.4.2 Normalized Root Mean Square Error

To compare the temperature data between the IRI and computed temperature images, the normalized root mean square (RMS) error will be implemented on the reduced matrix. Since the normalized RMS error is used to find the deviation between data, it is used to analyze the temperature difference between the two temperature values. The normalized RMS value is chosen as the comparison parameter since it is one of the most commonly used statistical parameter in heat transfer applications. The normalization is done with respect to the maximum scale given by the difference between the core body temperature and ambient temperature applied to the digital breast model. The normalized RMS error is given by the following equation:

$$RMSE_{Normalized} = \frac{\sqrt{\frac{\sum[(T_{IRI})_{i,j} - (T_{num})_{i,j}]^2}{N \times M}}}{T_c - T_\infty} \times 100\% \quad (12)$$

where $(T_{IRI})_{i,j}$ is the temperature of the IRI image at the entry (i,j), $(T_{num})_{i,j}$ is the temperature of the computed temperature images at the entry (i,j), $N \times M$ is the size of the temperature matrix, T_c is the core temperature, and T_∞ is the ambient temperature. This gives a single normalized RMS error value, which tells how far apart the computed temperature image is from the IRI image. This must be done to all pairs of thermal parameters, which is why a system is implemented to keep track of the pairing. This is done by assigning a pair of numbers to the tissue thermal conductivity (k) values and the blood perfusion rates ω_t and ω_h values. This allows for computed temperature images to be saved under the name k_p and ω_q, where p is the number for the thermal conductivity and q is the number for the blood perfusion rate. This allows for the process to be automated and run iteratively in MATLAB by storing the minimized RMS error results in a separate matrix of size $p \times q$. Then, the minimum RMS error can be obtained for each case which allows us to find the optimal thermal parameter pair for each case.

5 Results

In this chapter, results from mathematical analysis of the thermal parameters in Pennes' bioheat equation and the results for the parametric study of the thermal parameters in both the healthy and cancerous regions of a cancerous breast are presented. Each result, except the mathematical analysis, is separated into two parts (case 1 and case 2 as described is section 4.2.1). As previously stated in section 4.1, 30 biopsy-proven breast cancer patients were imaged at RGH using MRI and IRI. Out of these 30 patients, one patient was selected as the subject under study and two IRI image views of the cancerous breast were selected to conduct the parametric study. Although this study was conducted on one patient and on only one breast, the method presented in section 4 can be implemented on all 30 patients and on both breasts. Also, this study can be implemented on all eight IRI image views. The current work is focused on developing the algorithm to conduct parametric analysis using two views of any patient breast.

The subject under study, subject 3, is a biopsy-proven breast cancer patient with IDC and was selected due to the available clinical information. Detailed pathology data can be seen in Table 5. The algorithm successfully detected and localized the tumor in the previous study. In that study, evaluations were done on the multiview IRI images of both breasts. For this work, only two IRI images for the right breast will be used. Figure 16 shows the IRI image views that were selected for the parametric study. These two views were chosen due to the clearness of where there are gradual temperature differences and hotspot regions. Also, view 1 was selected due to the difference in orientation which will be further discussed in section 5.2. A flowchart of the method illustrated in Fig. 17 and discussed in chapter 4 is implemented on this subject. It includes the generation of the digital breast model as well since this part was recreated to validate the previous work.

Table 5: *Clinical information of subject 3 adapted from [23, 27].*

Patient Details			**Tumor Placement**			**Tumor Pathology**					**Thermal Property**
Age	Breast with Tumor	Breast Density	Tumor Depth	Tumor Diameter (cm)	Position in the breast	Cancer Type	ER+ or ER-	PR+ or PR-	HER2 + or HER2 -	Histologic Grade	Metabolic Heat Generation (W/m^3)
71	R	PF	*Anterior*	0.9×0.6×0.9	*10:00*	*IDC*	ER+	PR+	HER2-	1	65400

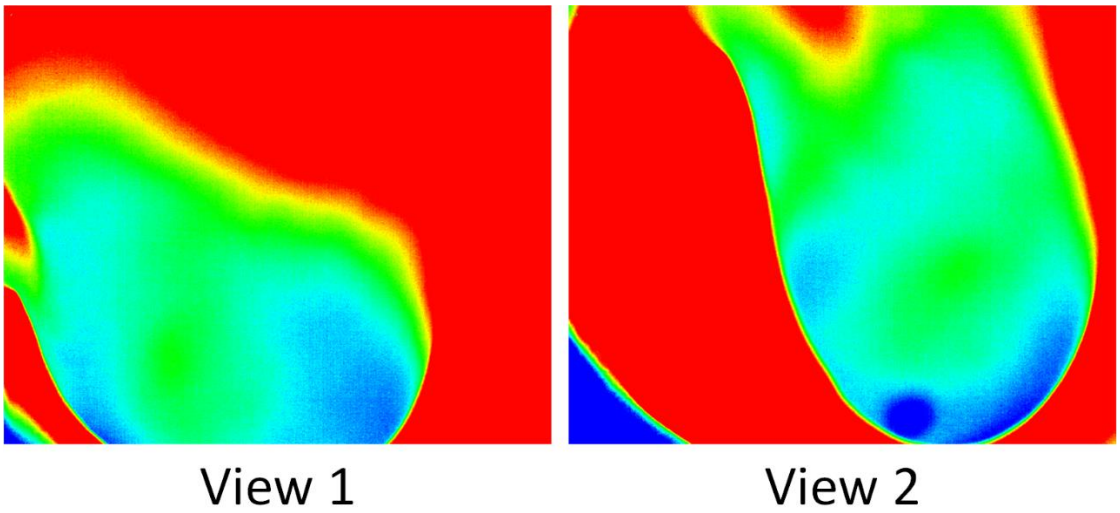

Figure 16: *Two clinical IRI images of the right breast of subject 3 used for this work.*

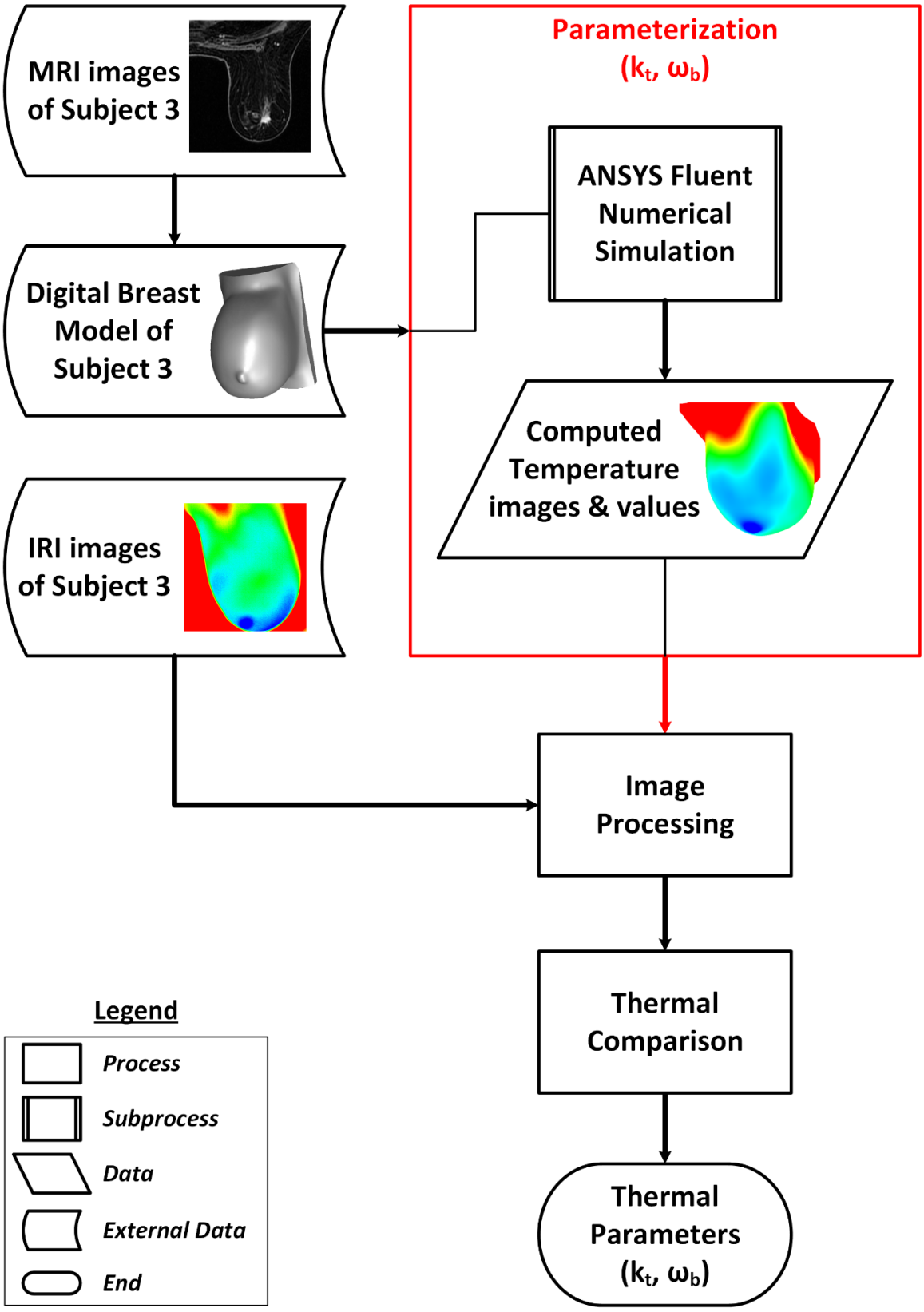

Figure 17: *Flow chart of the method used in the present work.*

5.1 Mathematical Analysis on Thermal Parameters

The thermal parameters can be mathematically studied through analytical techniques on the governing equations. Such techniques involve analyzing the type of Partial Differential Equation (PDE), functional behavior techniques, and optimization techniques on the analytic solution. For this work, only the first two techniques will be implemented to understand the behavior of these thermal parameters. The last technique may not be feasible due to the complexity of the geometry and system of equations applied to that geometry. The equation of study is the general Pennes' bioheat equation, which will need to be simplified to conduct these techniques.

$$\nabla \cdot (k\nabla T) + \rho_b c_b \omega (T_a - T) + Q = 0$$

Dividing both sides by the thermal conductivity k and using the substitutions

$$\alpha = \frac{k}{\rho_b c_b} \tag{13}$$

$$S = \frac{Q + \rho_b c_b \omega T_a}{k} \tag{14}$$

$$u = \frac{\omega}{\alpha} T - S \tag{15}$$

gives the following 3-D Helmholtz equation:

$$\nabla^2 u - \frac{\omega}{\alpha} u = 0 \tag{16}$$

Equation 16 is a linear homogeneous elliptic PDE with the second term in the equation acting as a dampening term. Since the dampening term is negative, this means that this term is what is helping the solution stabilize faster especially since both α and ω are positive values. If the thermal conductivity is increased to the point where $k \to \infty$, which will make $\alpha \to \infty$, then $\frac{\omega}{\alpha} u \to 0$. This

means that the equation will turn into the Laplace equation, which is known as the equilibrium equation. Solutions to this equation involve sinusoidal or oscillatory functions multiplied with hyperbolic or exponential functions, which the parameters have no effect on. Typically, because of the nature of the problem, it is multiplied with a decreasing exponential function so that it may reach a stability. Conversely, as perfusion rate increases to the point where $\omega \to \infty$, then $\frac{\omega}{\alpha} u \to \infty$ meaning that the dampening term becomes the dominating factor for the equation to reach stability.

Applying the substitutions, equations 13-15, to the boundary conditions in section 4.1.3 gives the following boundary conditions for equation 16:

$$\left.\frac{\partial u}{\partial \boldsymbol{n}}\right|_{A,B,C,D} = 0$$

$$u_E = u_0$$

$$Au + B\left.\frac{\partial u}{\partial \boldsymbol{n}}\right|_F = g$$

where $A = \frac{h\alpha}{\omega}$, $B = \frac{k\alpha}{\omega}$, and $g = h(T_\infty - \frac{\alpha}{\omega} S)$. Using separation of variables and the first boundary condition, a general analytic solution to the 3-D Helmholtz equation is obtained. Then, through backwards substitution using equations 13-15, the general solution to Pennes' bioheat equation is

$$T(x,y,z) = \frac{k}{\rho_b c_b \omega} \sum_{n=0}^{\infty} \sum_{m=0}^{\infty} \left(A_{nm} e^{\lambda_{nm} y} + B_{nm} e^{-\lambda_{nm} y}\right) \cos\left(\frac{n\pi x}{W}\right) \cos\left(\frac{m\pi z}{H}\right) + \frac{Q}{\rho_b c_b \omega} + T_a$$

where A_{nm} and B_{nm} are unknown constants, W and H are the respective width and height of the computational domain discussed in section 4.1.3, and $\lambda_{nm} = \sqrt{\frac{\rho_b c_b \omega}{k} + \left(\frac{n\pi x}{W}\right)^2 + \left(\frac{m\pi z}{H}\right)^2}$. Due to the maximum principal of elliptic PDEs, it can be concluded that constants A_{nm} must be small

enough or zero for the temperature to reach equilibrium. The other boundary conditions can also be used to solve for the constants, but these are not of much importance for the functional analysis.

When the perfusion rate is increased to the point where $\omega \to \infty$, the summation values go to zero as well as the second term leaving $T(x, y, z) = T_a$. This proves that as $\omega \to \infty$, then the dampening term takes over and dampens it to the artery temperature. When the thermal conductivity is increased to the point where $k \to \infty$, then the exponential terms approach 1. This leaves us with the constant terms and the nodal summation cosine functions multiplied with k. Due to the nature of these nodal functions they oscillate at different frequencies, but a minimum is always reached. This minimum value is dependent on the amplitude or constants multiplied to them as shown in Fig. 18. This means that as $k \to \infty$ the minimum for $T(x, y, z) \to -\infty$ and is shifted up by the second and third term.

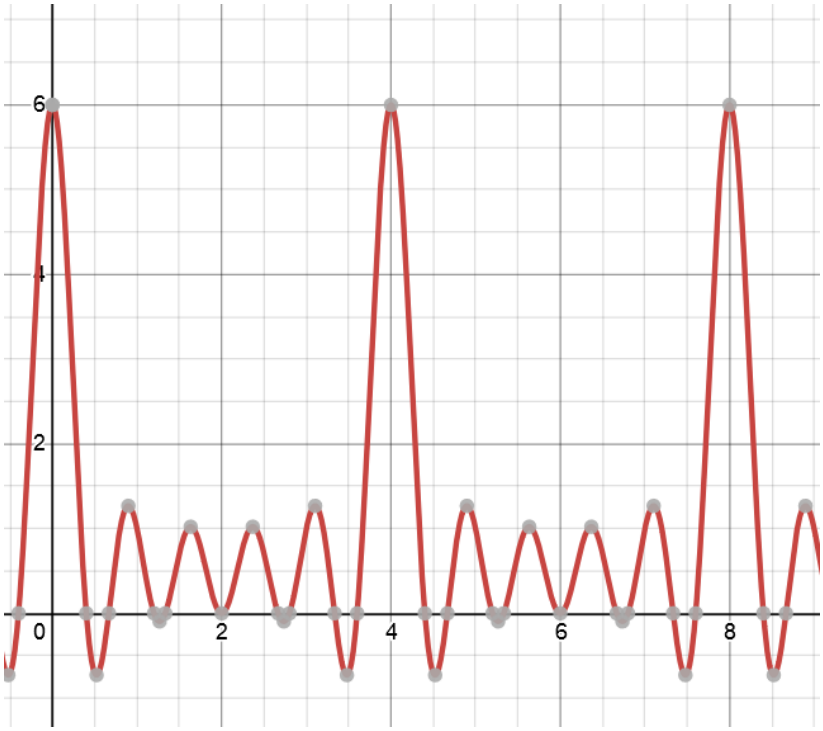

Figure 18: *Example of a nodal function graphed on Desmos with minimum and maximum values oscillating periodically.*

5.2 Parametrization

The digital breast model for this subject, Fig. 19, was recreated using the method discussed in section 4.1. Using the modified numerical simulation discussed in section 4.2, computed temperature images were obtained for different pairs of tissue thermal conductivity values and blood perfusion rates. The range values for the tissue thermal conductivity and blood perfusion rate of the tumor and surrounding tissue are shown in Table 6. These ranges are derived from recommendations made in Gautherie's work [24]. The range of tissue thermal conductivity values chosen correspond to the breast density type of subject 3, which is predominantly fatty. As stated in section 4.2, breasts that are considered fatty have a thermal conductivity range of 0.100 W/mK to about 0.200 W/m·K. For the tumor blood perfusion rate, the values reported by Gautherie for healthy tissue blood perfusion and cancerous tissue blood perfusion rate were used to arrive at the stated ranges. Once this was established, all ranges were incremented at small intervals, which will be discussed in this section. Then, the system created in section 4.4 to keep track of the pairing is implemented in the algorithm. For example, case 1 simulation 37 corresponds to tissue thermal conductivity $k_1 = 0.1\ W/mK$ with tumor blood perfusion rate $\omega_{37} = 9 \times 10^{-3}$ s^{-1}, etc.

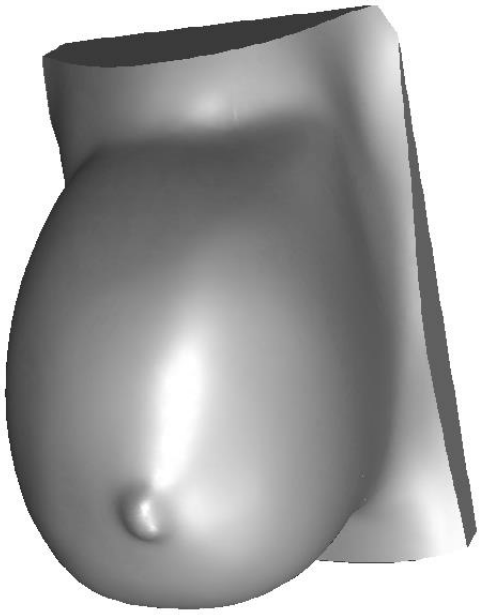

Figure 19: *Patient-specific digital breast model of the right breast of subject 3.*

Table 6: *Range of thermal parameters for parametric study*

Parameter	Range	Unit
Thermal conductivity of breast tissue (k)	0.100 – 0.180	W $m^{-1}K^{-1}$
Blood perfusion rate of tumor (ω_t)	1.8×10^{-4} – 9×10^{-3}	s^{-1}
Blood perfusion rate of surrounding tissue (ω_h)	1.2 – 3.6×10^{-4}	s^{-1}

5.2.1 Analytical Parameterization of Case 1 – Effect of tumor perfusion rate

The purpose of the parametrization study is to identify the set of thermal conductivity and blood perfusion rate values that provide accurate match between the simulated thermal images and the IRI images. For the first case of simulations, the thermal conductivity values were incremented at 5×10^{-3} W/m·K intervals giving a total of 17 thermal conductivity values ($k_1 - k_{17}$). The tumor blood perfusion rate values were incremented at values of 1.47×10^{-4} s^{-1} for 1.8×10^{-4} s^{-1}-1.944×10^{-3} s^{-1} and increments of 2.94×10^{-4} s^{-1} for values until 9×10^{-3} s^{-1} giving a total of 37 perfusion rate values ($\omega_1 - \omega_{37}$). This gives a total of 629 pairs that were first numerically

simulated. The blood perfusion rate of the surrounding breast tissue was held constant at 1.8×10^{-4} s^{-1}. Initially, thermal conductivity and perfusion rate values up to 0.28 W/mK and 3.6×10^{-2} s^{-1}, respectively, were tested but the higher values were later disregarded since these values did not match the breast tissue type and were outside the range of blood perfusion rate of a tumor.

The computed temperature images show the effects of varying both thermal parameters. Figure 20 shows the computed temperature images of both views for tissue thermal conductivities 1, 5, 11, and 17 at blood perfusion rate 21. The images show a decrease in temperature distribution on the surface when the perfusion rate value is fixed, and thermal conductivity value is increased. This is shown for both views with view 2 (first row) having a more noticeable distinction than view 1 (second row).

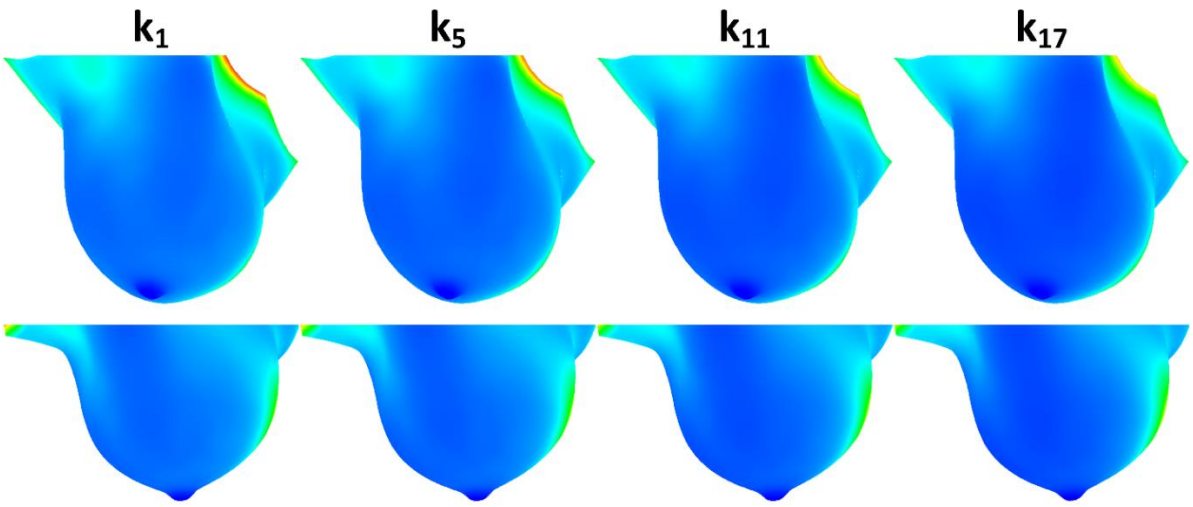

Figure 20: *Computed temperature images of subject 3 at view 2 (top row) and 1 (bottom row) for thermal conductivity 1, 5, 11, and 17 ($k_{1,5,11,17}$=0.100, 0.120, 0.150, and 0.180 W/mK, respectively) all at perfusion rate 21 ($\omega_{21} = 4.296 \times 10^{-3}$ s^{-1}).*

Similarly, Fig. 21 shows the computed temperature images of both views for thermal conductivity 3 at perfusion rates 1, 9, 23, and 37. These images show the temperature distribution increasing when fixing the tissue thermal conductivity and increasing the tumor blood perfusion rate, but with less noticeable distinction from perfusion rate 1 to 9 or from 23 to 37. These two figures match what is observed in the analytic solution presented in section 5.1, which displays the accuracy in the model. However, it is not as clear in understanding what the tumor blood perfusion rate variation is contributing.

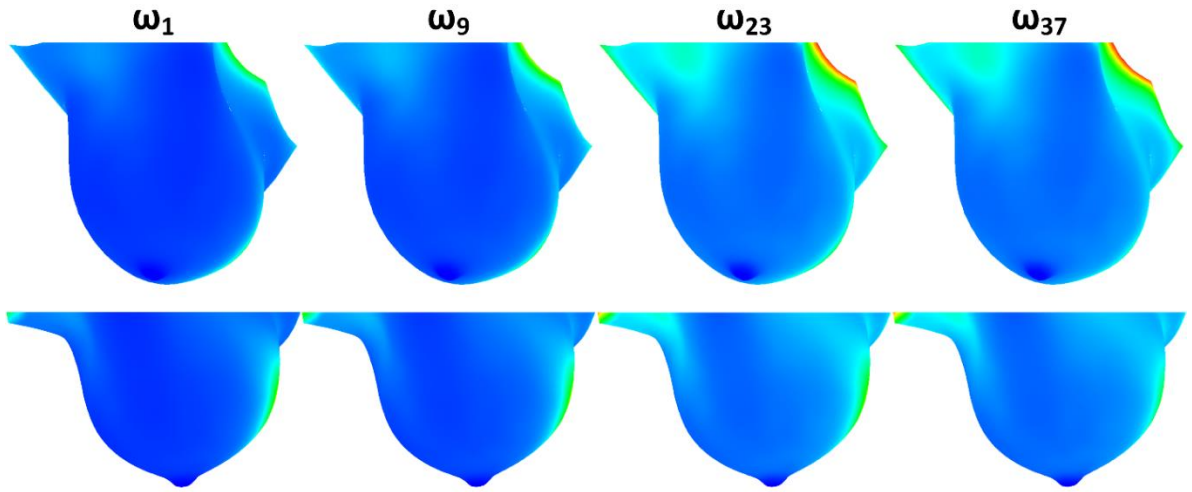

Figure 21: *Computed temperature images of subject 3 at view 2 (top row) and 1 (bottom row) at perfusion rates 1, 9, 23, and 37 ($\omega_{1,9,23,37}$= $1.8 \times 10^{-4}, 1.356, 4.884, and\ 9 \times 10^{-3}$ s^{-1}, respectively) all for thermal conductivity 3 ($k_3 = 0.110$ W/m·K).*

5.2.2 Analytical Parameterization of Case 2 – Effect of Blood Perfusion Rate in Breast Tissue

As stated in the previous section, the purpose of the parametrization study is to identify the set of thermal conductivity and blood perfusion rate values that provide accurate match between the simulated thermal images and the IRI images. This section gives the details of the effect of varying perfusion rate in the breast tissue on the accuracy of prediction using the IRI images. For this second case of simulations, the same range for tissue thermal conductivity values from case 1 were used but incremented at 0.01 W/m·K intervals giving a total of 9 thermal conductivity values ($k_1 -$

k_9). The range of the blood perfusion rate of the surrounding breast tissue shown in Table 6 were incremented at values of 0.2×10^{-4} s^{-1} giving a total of 13 perfusion rate values ($\omega_1 - \omega_{13}$). The tumor blood perfusion rate will be selected based on the results that will be shown in section 5.4.1, the pathology of the tumor, and the vasculature observed in the MRI images. It may be noted that the blood perfusion rate values in the breast tissue are generally much lower than those for the tumors.

Figures 22 and 23 show the computed temperature images for case 2. In contrast with what observed for case 1, the images show an increase in temperature distribution on the surface when the blood perfusion rate value is fixed, and thermal conductivity value is increased, but this increase is slight. Also, similar to case 1, the images show an increase in temperature distribution on the surface when the tissue thermal conductivity is fixed, and the blood perfusion rate of the tissue is increased. Although there is an obvious difference, the effects are not clear enough to make any concrete conclusions. Therefore, the statistical outcomes will be analyzed to make any conclusions.

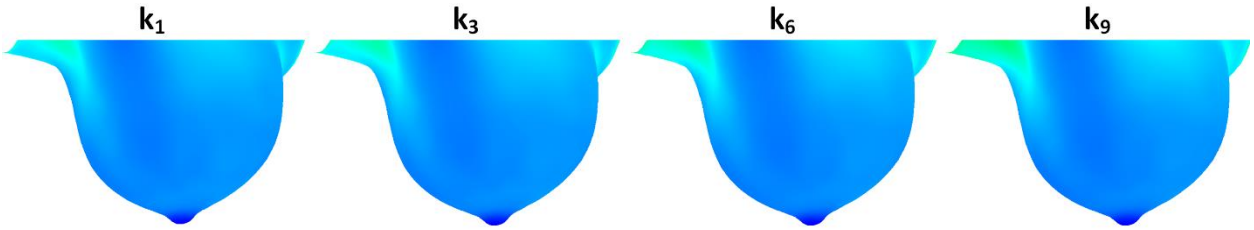

Figure 22: *Computed temperature images of subject 3 at view 1 for thermal conductivity 1, 3, 6, and 9 ($k_{1,3,6,9}$=0.100, 0.120, 0.150, and 0.180 W/m·K, respectively) all at perfusion rate 9 ($\omega_9 = 2.8 \times 10^{-4}$ s^{-1}).*

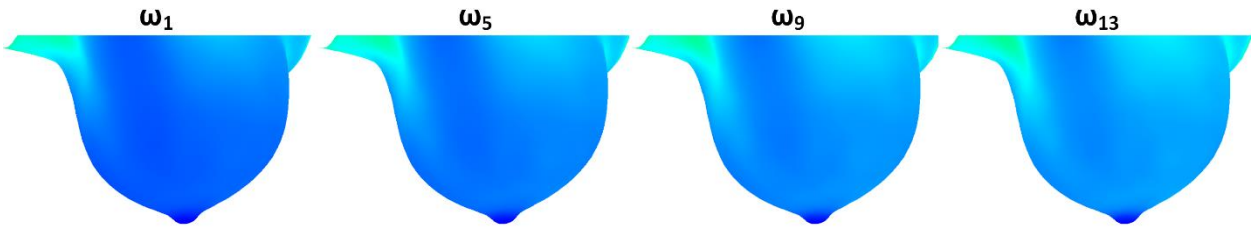

Figure 23: *Computed temperature images of subject 3 at view 1 at perfusion rates 1, 5, 9, and 13 ($\omega_{1,5,9,13}$= 1.2, 2.0, 2.6, 3.4 and 9×10^{-4} s^{-1}, respectively) all for thermal conductivity 3 ($k_5 = 0.14$ W/m·K).*

5.3 Image Processing

After the computed temperature images were obtained, the image processing method discussed in section 4.3 was implemented after the calibration process. The calibration process was done using the original numerical simulation method recreated from Gonzalez-Hernandez et al. [23, 27] for this subject. The results of the calibration on the IRI and computed temperature images for views 1 and 2 are shown in Fig. 24 and Fig. 25, respectively. Figure 24 shows the importance of view 1 as it tested the capabilities of MATLAB's image registration algorithm. This method was then applied to all computed temperature images obtained from the modified numerical simulation. Once this was done, the ROI was selected from the two IRI grayscale images and then the registered images are cropped to the size of the ROI, as discussed in section 4.3.

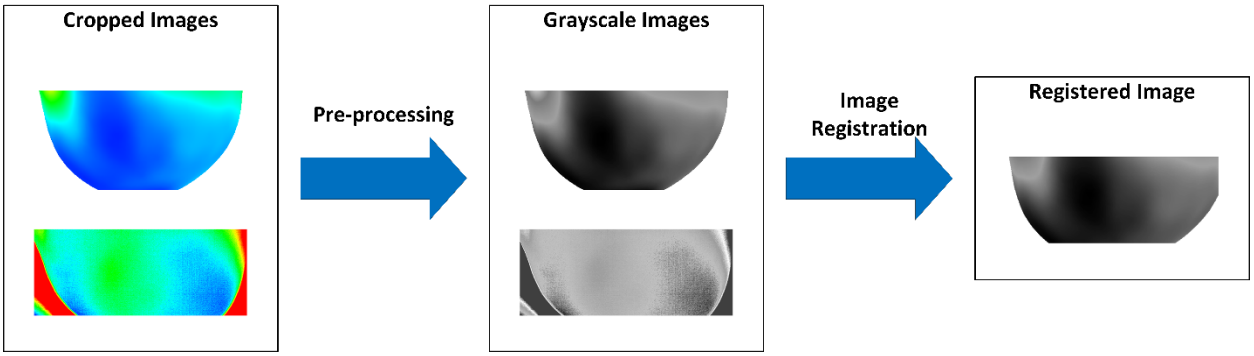

Figure 24: *Calibration image processing step of original numerical simulation computer temperature images for view 1.*

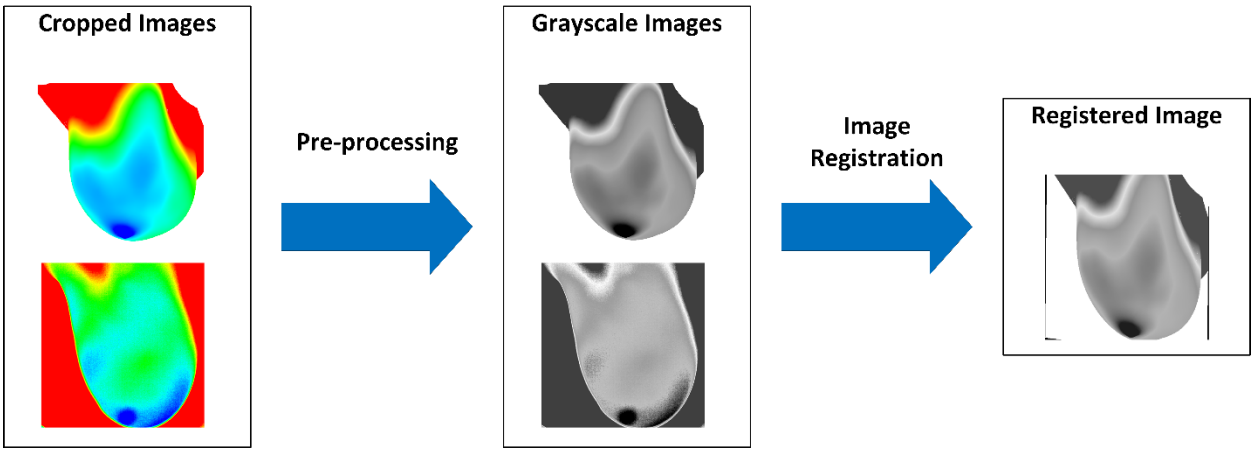

Figure 25: *Calibration image processing step of original numerical simulation computer temperature images for view 2.*

5.4 Thermal Comparison

Once these cropped ROI images were obtained, temperature values were assigned to each pixel based on the method discussed in section 4.4. For view 1, the cropped ROI images had a pixel count of 101×186 while view 2 had a pixel count of 242×278. The minimum and maximum temperature values in the ROI for the IRI of view 1 is 27.080ºC and 27.855ºC, respectively, and 27.120ºC and 27.989ºC for view 2. Although the accuracy of measurements does not justify using three decimal accuracy, this is done to reduce round off errors. These values may be considered to be accurate within only the first decimal value. For the computed temperature images, each minimum and maximum temperature values for each pair was recorded in an excel table. This gave a 101×186 matrix for view 1 and a 242×278 matrix for view 2 with temperature values as the entries of the matrix for each image. Once the temperature values were assigned to the pixels, the filtering technique discussed in section 4.4 was implemented giving a 50×93 matrix for view 1 and a 121×139 matrix for view 2 with the mean temperature values as the matrix entries.

5.4.1 Numerical Comparison for Case 1 – Effect of Blood Perfusion Rate in Tumor

The normalized RMS error was calculated between the IRI and computed temperature values and plotted against the tumor blood perfusion rate in the tumor as shown in Fig. 26. Oscillatory behavior can be observed from the graph, which is due to noise coming from the computed temperature images. From these plots, it can be observed that as tissue thermal conductivity increases, the normalized RMS error decreases. Also, varying the tumor perfusion rate does not have any impact on the heat transfer and thermal profile as seen from the computed thermal profiles. The oscillations seen in this plot are random in nature and are believed to be due to noise.

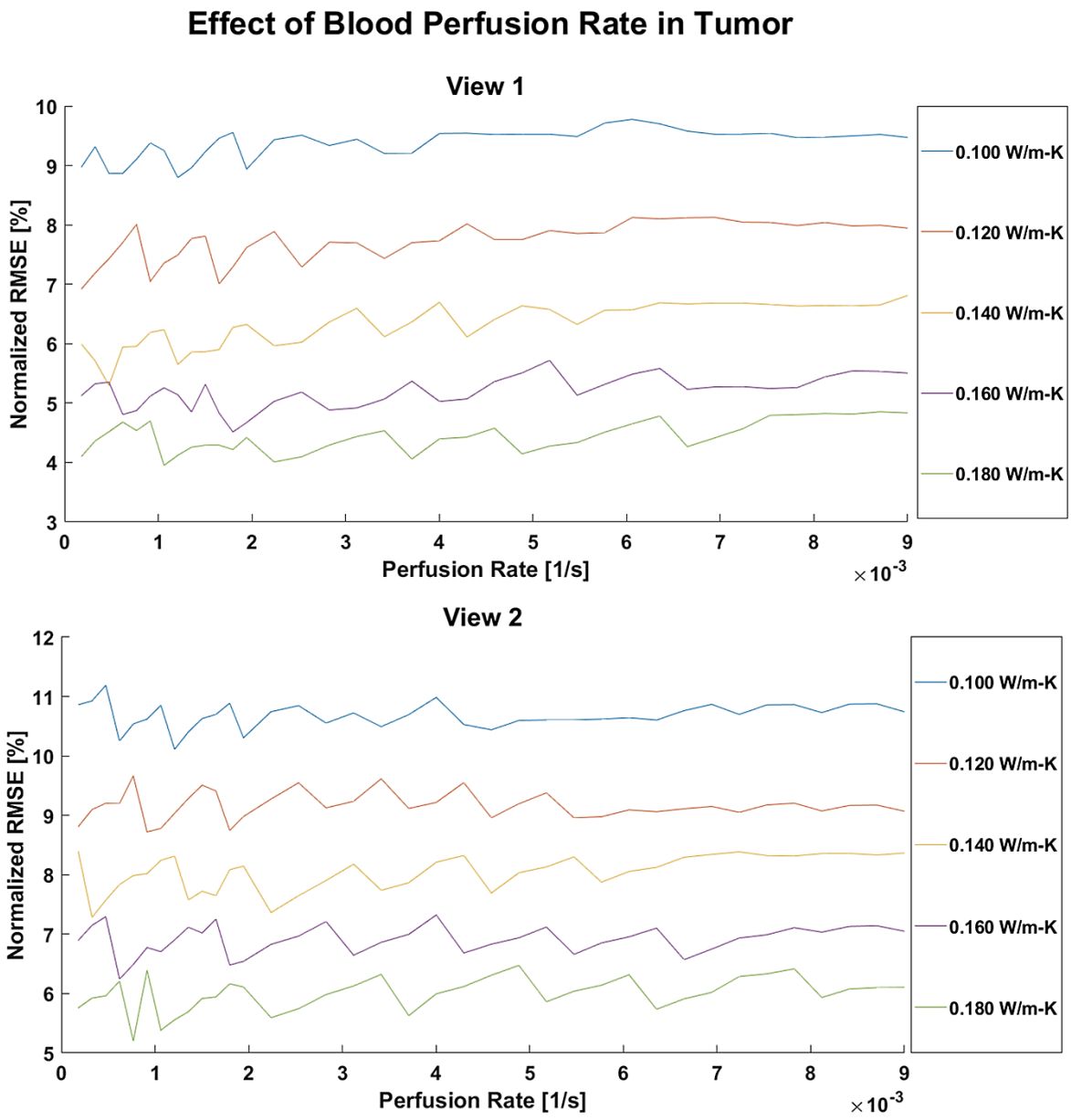

Figure 26: *Results of normalized RMS error plotted over different blood perfusion rates in tumor at thermal conductivity 1, 5, 9, 13, and 17 for both views.*

These results verify that the tumor blood perfusion rate has no effect on the thermal profile. This is reasonable as the tumor generates a certain amount of heat which enters into the breast from tumor boundaries. Any internal temperature gradients within the tissue are of no consequence in the heat transfer from the tumor boundaries.

5.4.2 Numerical Comparison for Case 2 – Effect of Blood Perfusion Rate in the Breast Tissue

For the second case, the blood perfusion rate value in the tumor of 5.178×10^{-3} s^{-1} was selected from case 1 due the vasculature observed from the MRI image of subject 3 shown in Fig. 27. It should be recognized that the value of the blood perfusion rate in the tumor has no effect on the thermal profile as seen from the case 1 results and this selection is not expected to have any influence on the results. Also, the simulations were implemented on only view 1 as this view was seen to have less noise than view 2. The normalized RMS error was calculated and plotted versus the blood perfusion rate of the surrounding breast tissue for each case as shown in Fig. 28. From this plot, it can be observed there are minimum values with the plot first decreasing to a minimum and then increasing as the blood perfusion rate increases. When plotting the minimum normalized RMS error per thermal conductivity, the minimum values for each tissue thermal conductivity value is obtained at different blood perfusion rates of the surrounding breast tissue. It is seen from the plot that the minimum value of the normalized RMS is approximately the same around 2% for all thermal conductivity values. It may be concluded that the optimum value of blood perfusion rate of the surrounding breast tissue depends on the tissue thermal conductivity as several combinations yield results close to optimum value. Further work is needed to establish this relationship.

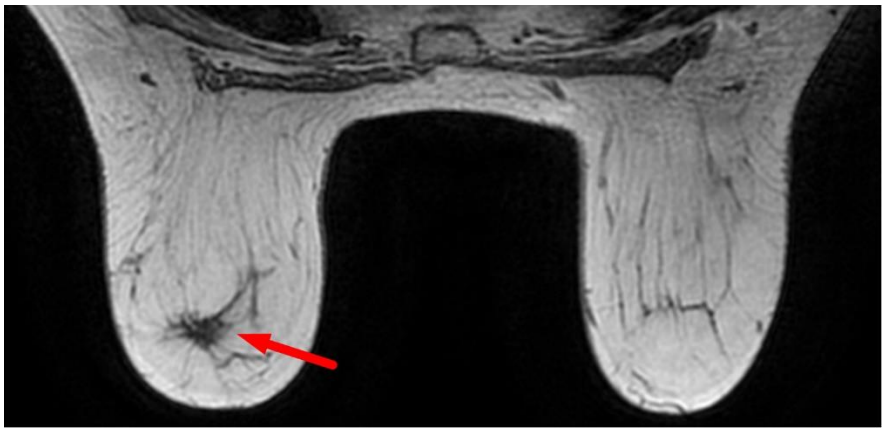

Figure 27: *MRI image of subject 3 with an observable tumor that has an abnormal vasculature.*

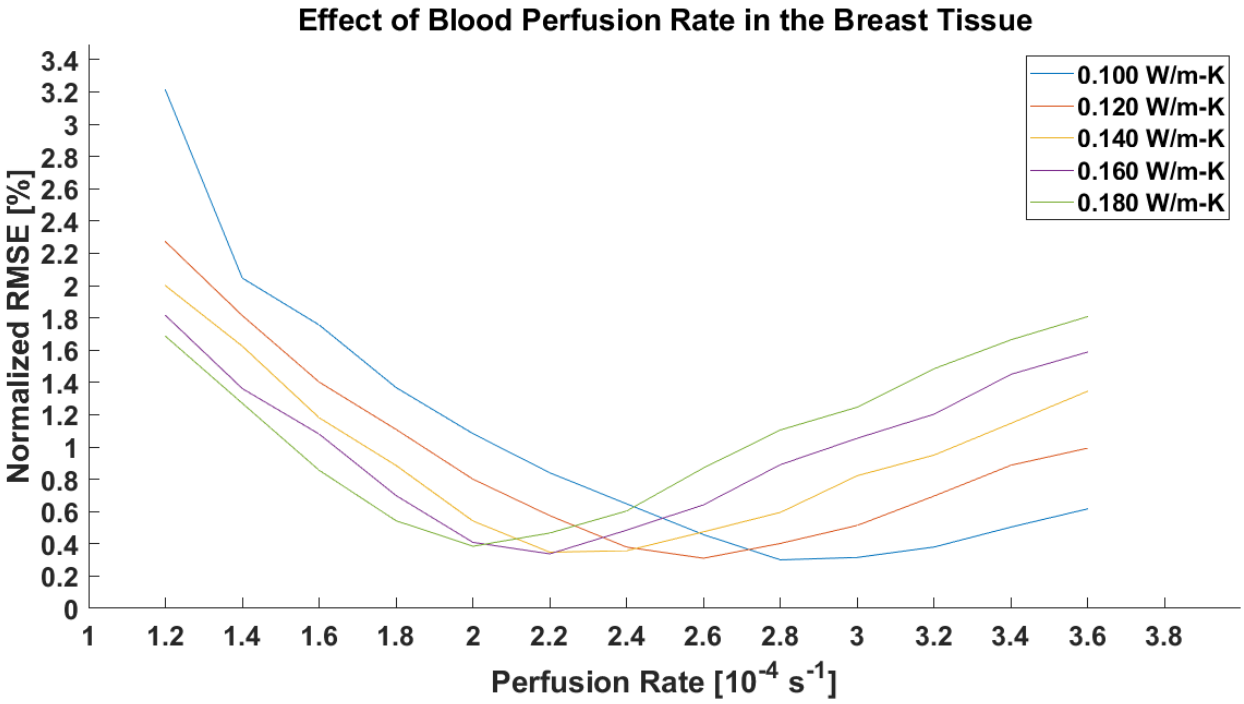

Figure 28: *Plot of blood perfusion rate of surrounding breast tissue versus normalized RMS error for thermal conductivity 1, 3, 5, 7, and 9 for view 1*

6 Discussion

In this study, a patient-specific digital breast model of subject 3 was recreated using the method from Gonzalez-Hernandez et al. [22]. This model was used to perform study of thermal parameters (i) tissue thermal conductivity, (ii) tumor blood perfusion rate, and (iii) surrounding tissue blood perfusion rate on the heat transfer within the breast and comparison with the clinical IRI images. It was intended to obtain the optimum combinations of properties that yielded the best match with clinical IRI images. This was accomplished through a modifications of the numerical simulation software and UDF created by Gonzalez-Hernandez et al. [22] as well as the image registration process [23].

As mentioned in chapter 5, this study can be conducted on all 30 patients, regardless of breast density type, and on both breasts. Although this technique worked well for both positions, view 1 was much more difficult to register and did not register as well as view 2, as seen in Fig. 25. Position 1 was easier to register due to the algorithm using the nipple as a guide, while position 2 did not have any sort of guide and it was based more on curvature of the breast. The image registration process can be an issue, as the alignment process for the computer temperature images is a long manual process. For obtaining the temperatures at the ROI, a better technique can be implemented to reduce any error as these values were obtained by visual inspection using the calibrated images.

The results indicate that the tumor blood perfusion rate has no effect on the simulated thermal profile. The surrounding tissue blood perfusion rate has considerable effect on the simulated thermal profile. The minimum value of the RMS error between the simulated and profile and IRI images varies with the thermal conductivity. As the thermal conductivity increases, the value of the surrounding tissue perfusion rate decreases at the minimum error condition.

The analysis indicates that the program can be used for studying the effect of thermal properties of the tissue on thermal profiles on the breast surface. This technique may be used in an inverse program to determine thermal properties in cases where they are not available. This could serve as a useful tool for future research.

7 Conclusions

A parametric analysis was performed to study the effects of tissue thermal conductivity, and blood perfusion rates in tumor and the surrounding tissue. The available algorithm and program from a previous study was modified to accomplish this analysis.

The values for the appropriate pairs of thermal parameters for the simulation were selected as the ranges 0.1- 0.18 W/m·K for the tissue thermal conductivity, 1.8×10^{-4}-9.0×10^{-3} s^{-1} for the blood perfusion rate of a tumor, and $1.2 - 3.6 \times 10^{-4}$ s^{-1} for the blood perfusion rate of the surround breast tissue based on Gautherie's recommendations . These values lie in the range reported by Gautherie [25] for a predominantly fatty breast density with an abnormal blood perfusion due to a carcinoma and a high metabolic heat generation in the tumor.

It is seen from this study that the blood perfusion rate in the tumor does not have any effect on the thermal profile. This is expected since the tumor generates heat that is transferred at the tumor boundaries irrespective of its vasculature and thermal conductivity. These values will have influence on the temperature distribution within the tumor. However, we are not interested in the temperature distribution inside the tumor.

Another major conclusion is that as the thermal conductivity of the surrounding tissue increases, the location of minimum error between the simulated and IRI images shifts to higher blood perfusion rates in the surrounding tissue. The minimum error for all such pairs appears to be approximately same at around 2%. Further work is needed to establish the relationship between thermal conductivity and blood perfusion rate in the surrounding tissue that provides the most accurate simulation.

8 Suggested Future Work

In the present work, a technique to study the effect of varying thermal parameters of patients with known breast tumor size and location through a parametric study approach was created using IRI images and computational techniques. This technique serves as a preliminary step to future work relating to thermopathological studies of breast carcinomas. Next steps for future work would be as follows:

- Automating the process by creating a link between the numerical simulation and image processing steps so that the program has a reduced amount of human interaction time
- Creating digital breast models from the multiview IRI images using volumetric and spatial data from a clinically acceptable scanner for easier and precise image registration
- Generating phantom models similar to those created by Gautherie [25] to validate the heat transfer phenomena observed in this study
- Mapping vascular networks and exploring hierarchical approaches to the model for further validation and findings
- Conducting the study on other carcinomas in a different location where it may be easier to obtain measurements

These next steps will allow for further studies and correlations to be conducted on the thermopathology of cancers as well as expand the use of IR thermography as a noninvasive tool in cancer research.

9 References

[1] "Breast Cancer," American Cancer Society, [Online]. Available: https://www.cancer.org/cancer/breast-cancer.html. [Accessed 26 10 2019].

[2] B. J. Tromberg, B. W. Pogue, K. D. Paulsen, A. G. Yodh, D. A. Boas and A. E. Cerussi, "Assessing the future of diffuse optical imaging technologies for breast cancer management," *Medical Physics,* vol. 35, no. 6 part 1, pp. 2443-2451, 2008.

[3] S. Mallidi, G. P. Luke and S. Emelianov, "Photoacoustic imaging in cancer detection, diagnosis, and treatment guidance," *Trends in biotechnology,* vol. 29, no. 5, pp. 213-221, 2011.

[4] Z. Ji, C. Lou, S. Yang and D. Xing, "Three-dimensional thermoacoustic imaging for early breast cancer detection," *Medical physics,* vol. 39, no. 11, pp. 6738-6744, 2012.

[5] "The Breast (Human Anatomy): Picture, Function, Conditions, & More," WebMD, [Online]. Available: https://www.webmd.com/women/picture-of-the-breasts. [Accessed 9 July 2020].

[6] "Anatomy of the Breast | Memorial Sloan Kettering Cancer Center," [Online]. Available: https://www.mskcc.org/cancer-care/types/breast/anatomy-breast. [Accessed 07 July 2020].

[7] "About Breast Cancer," National Breast Cancer Foundation, Inc, [Online]. Available: https://www.nationalbreastcancer.org/early-detection-of-breast-cancer/. [Accessed 22 October 2019].

[8] UCHealth, "How Accurate Are Mammograms?," UCHealth, 6 July 2015. [Online]. Available: https://www.uchealth.org/today/how-accurate-are-mammograms/. [Accessed 3 Novemeber 2019].

[9] K. P. Tan, Z. A. Mohamad, M. P. Rumaisa, M. R. A. M. Siti, S. Radhika, M. I. Nurismah, A. Norlia and M. A. Zulfiqar, "The comparative accuracy of ultrasound and mammography in the detection of breast cancer," *The Medical journal of Malaysia,* vol. 69, no. 2, pp. 79-85, 2014.

[10] G. L. G. Menezes, F. M. Knuttel, B. L. Stehouwer, R. M. Pijnappel and M. A. A. J. van den Bosch, "Magnetic resonance imaging in breast cancer: a literature review and future perspectives," *World journal of clinical oncology,* vol. 5, no. 2, p. 61, 2014.

[11] breastcancer.org, "Breast MRI for Screening," breastcancer.org, 8 September 2016. [Online]. Available: https://www.breastcancer.org/symptoms/testing/types/mri/screening. [Accessed 3 November 2019].

[12] J. C. M. van Zelst, S. Vreemann, H.-J. Witt, A. Gubern-Merida, M. D. Dorrius, K. Duvivier, S. Lardenoije-Broker, M. B. I. Lobbes, C. Loo, W. Veldhuis and others, "Multireader study on the diagnostic accuracy of ultrafast breast magnetic resonance imaging for breast cancer screening," *Investigative radiology,* vol. 53, no. 10, pp. 579-586, 2018.

[13] T. Huzarski, B. Gorecka-Szyld, J. Huzarska, G. Psut-Muszynska, G. Wilk, R. Sibilski, C. Cybulski, B. Kozak-Klonowska, M. Siolek, E. Kilar and others, "Screening with magnetic resonance imaging, mammography and ultrasound in women at average and intermediate risk of breast cancer," *Hereditary cancer in clinical practice,* vol. 15, no. 1, p. 4, 2017.

[14] R. Usamentiaga, P. Venegas, J. Guerediaga, L. Vega, J. Molleda and F. G. Bulnes, "Infrared Thermography for Temperature Measurement and Non-Destructive Testing," *Sensors,* vol. 14, no. 7, pp. 12305-12348, 2014.

[15] Y. Fu, J.-x. Ni, F. Marmori, Q. Zhu, C. Tan and J.-p. Zhao, "Infrared thermal imaging-based research on the intermediate structures of the lung and large intestine exterior-interior relationship in asthma patients," *Chinese journal of integrative medicine,* vol. 22, no. 11, pp. 855-860, 2016.

[16] A. Szentkuti, H. Skala Kavanagh and S. Grazio, "Infrared Thermography and Image Analysis for Biomedical Use," *Periodicum Biologrum,* vol. 113, no. 4, pp. 385-392, 2011.

[17] E. F. J. Ring and K. Ammer, "Infrared thermal imaging in medicine," *Physiological measurement,* vol. 33, no. 3, pp. R33-R46, 2012.

[18] X. Zhao, S. He and M. C. Tan, "Advancements in infrared imaging platforms: complementary imaging systems and contrast agents," *Journal of Materials Chemistry B,* vol. 5, no. 23, pp. 4266-4275, 2017.

[19] D. Cardone and A. Merla, "New frontiers for applications of thermal infrared imaging devices: Computational psychopshysiology in the neurosciences," *Sensors,* vol. 17, no. 5, p. 1042, 2017.

[20] S. G. Kandlikar, D. Dabudeen, L. Medeiros, P. Phatak, J. L. G. Hernandez and A. N. Recinella, "Detection and Characterization of Cancerous Tumors". United States of America Patent 16/439,192, 19 December 2019.

[21] J. L. Gonzalez-Hernandez, "A Patient-Specific Approach for Breast Cancer Detection and Tumor Localization Using Infrared Imaging," Thesis. Rochester Institute of Technology, 2019. [Online]. Available: https://scholarworks.rit.edu/theses/10212. [Accessed 2020].

[22] J.-L. Gonzalez-Hernandez, S. G. Kandlikar, D. Dabydeen, L. Medeiros and P. Phatak, "Generation and Thermal Simulation of a Digital Model of the Female Breast in Prone Position," *Journal of Engineering and Science in Medical Diagnostics and Therapy,* vol. 1, p. 041006, 2018.

[23] J. L. Gonzalez-Hernandez, A. N. Recinella, S. G. Kandlikar, D. Dabydeen, L. Medeiros and P. Phatak, "An inverse heat transfer approach for patient-specific breast cancer detection and tumor localization using surface thermal images in the prone position," *Infrared Physics & Technology,* vol. 105, p. 103202, 2020.

[24] H. H. Pennes, "Analysis of tissue and arterial blood temperatures in the resting human forearm," *Journal of applied physiology,* vol. 1, no. 2, pp. 93-122, 1948.

[25] M. Gautherie, "Thermopathology of breast cancer: measurement and analysis of in vivo temperature and blood flow," *Annals of the New York Academy of Sciences,* vol. 335, no. 1, pp. 383-415, 1980.

[26] M. Gautherie, "Thermobiological assessment of benign and malignant breast diseases," *American Journal of Obstetrics & Gynecology,* vol. 147, no. 8, pp. 861-869, 1983.

[27] A. N. Recinella, J. L. Gonzalez-Hernandez, S. G. Kandlikar, D. Dabydeen, L. Medeiros and P. Phatak, "Clinical Infrared Imaging in the Prone Position for Breast Cancer Screening—Initial Screening and Digital Model Validation," *Journal of Engineering and Science in Medical Diagnostics and Therapy,* vol. 3, no. 1, 2020.

[28] R. Lawson, "Implications of surface temperatures in the diagnosis of breast cancer," *Canadian Medical Association Journal,* vol. 75, no. 4, p. 309, 1956.

[29] H. J. Isard, W. Becker, R. Shilo and B. J. Ostrum, "Breast thermography after four years and 10,000 studies," *American Journal of Roentgenology,* vol. 115, no. 4, pp. 811-821, 1972.

[30] A. M. Stark and S. Way, "The screening of well women for the early detection of breast cancer using clinical examination with thermography and mammography," *Cancer,* vol. 33, no. 6, pp. 1671-1679, 1974.

[31] C. H. Jones, W. P. Greening, J. B. Davey, J. A. McKinna and V. J. Greeves, "Thermography of the female breast: a five-year study in relation to the detection and prognosis of cancer," *The British journal of radiology,* vol. 48, no. 571, pp. 532-538, 1975.

[32] M. Moskowitz, J. Milbrath, P. Gartside, A. Zermeno and D. Mandel, "Lack of efficacy of thermography as a screening tool for minimal and stage I breast cancer," *New England Journal of Medicine,* vol. 295, no. 5, pp. 249-252, 1976.

[33] K. L. Williams, B. H. Phillips, P. A. Jones, S. A. Beaman and P. J. Fleming, "Thermography in screening for breast cancer," *Journal of Epidemiology & Community Health,* vol. 44, no. 2, pp. 112-113, 1990.

[34] M. Moskowitz, S. H. Fox, R. B. del Re, J. R. Milbrath, L. W. Bassett, R. H. Gold and K. A. Shaffer, "The potential value of liquid-crystal thermography in detecting significant mastopathy," *Radiology,* vol. 140, no. 3, pp. 659-662, 1981.

[35] E. E. Sterns and B. Zee, "Thermography as a predictor of prognosis in cancer of the breast," *Cancer,* vol. 67, no. 6, pp. 1678-1680, 1991.

[36] G. D. Dodd, "Present status of thermography, ultrasound and mammography in breast cancer detection," *Cancer,* vol. 39, no. 6, pp. 2796-2805, 1977.

[37] M. Moskowitz, "Thermography as a risk indicator of breast cancer. Results of a study and a review of the recent literature," *The Journal of reproductive medicine,* vol. 30, no. 6, pp. 451-459, 1985.

[38] Center for Devices and Radiological Health, "FDA Warns Thermography Should Not Be Used in Place of Mammography to Detect, Diagnose, or Screen for Breast Cancer: FDA Safety Communication," *FDA,* 20 December 2019.

[39] T. Sella, M. Sklair-Levy, M. Cohen, M. Rozin, M. Shapiro-Feinberg, T. M. Allweis, E. Libson and D. Izhaky, "A novel functional infrared imaging system coupled with multiparametric computerised analysis for risk assessment of breast cancer," *European radiology,* vol. 23, no. 5, pp. 1191-1198, 2013.

[40] M. EtehadTavakol, V. Chandran, E. Y. K. Ng and R. Kafieh, "Breast cancer detection from thermal images using bispectral invariant features," *International Journal of Thermal Sciences,* vol. 69, pp. 21-36, 2013.

[41] A. E. Collett, C. Guilfoyle, E. J. Gracely, T. G. Frazier and A. V. Barrio, "Infrared imaging does not predict the presence of malignancy in patients with suspicious radiologic breast abnormalities," *The breast journal,* vol. 20, no. 4, pp. 375-380, 2014.

[42] S. G. Kandlikar, I. Perez-Raya, R. Pruthvik A., J.-L. Gonzalez-Hernandez, D. Dabydeen, L. Medeiros and P. Phatak, "Infrared imaging technology for breast cancer detection–Current status, protocols and new directions.," *International Journal of Heat and Mass Transfer,* vol. 108, pp. 2303-2320, 2017.

[43] J.-L. Gonzalez-Hernandez, A. N. Recinella, S. G. Kandlikar, D. Dabydeen, L. Medeiros and P. Phatak, "Technology, application and potential of dynamic breast thermography for the detection of breast cancer," *International Journal of Heat and Mass Transfer,* vol. 131, pp. 558-573, 2019.

[44] H. C. Bazett, E. S. Mendelson, L. Love and B. Libet, "Precooling of blood in the arteries, effective heat capacity and evaporative cooling as factors modifying cooling of the extremities," *Journal of Applied Physiology,* vol. 1, no. 2, pp. 169-182, 1948.

[45] H. C. Bazett, L. Love, M. Newton, L. Eisenberg, R. Day and R. Forster, "Temperature changes in blood flowing in arteries and veins in man," *Journal of Applied Physiology,* vol. 1, no. 1, pp. 3-19, 1948.

[46] Y. Xuan and W. Roetzel, "Bioheat Equation of the Human Thermal System," *Chemical Engineering & Technology: Industrial Chemistry-Plant Equipment-Process Engineering-Biotechnology,* vol. 20, no. 4, pp. 268-276, 1997.

[47] C. K. Charny, "Mathematical models of bioheat transfer," in *Advances in heat transfer*, 1992.

[48] A. Nakayama, F. Kuwahara and W. Lui, "Macroscopic governing equations for bioheat transfer phenomena," in *Proceedings of the Second International Conference on Porous Media and Its Application in Science and Engineering*, 2007.

[49] S. Mahjoob and K. Vafai, "Analysis of bioheat transport through a dual layer biological media," *Journal of Heat Transfer,* vol. 132, no. 3, p. 031101, 2010.

[50] L. Wang and J. Fan, "Modeling bioheat transport at macroscale," *Journal of Heat Transfer,* vol. 133, no. 1, p. 011010, 2011.

[51] Z.-Z. He and J. Liu, "A coupled continuum-discrete bioheat transfer model for vascularized tissue," *International Journal of Heat and Mass Transfer,* vol. 107, pp. 544-556, 2017.

[52] Z.-Z. He and J. Liu, "An efficient parallel numerical modeling of bioheat transfer in realistic tissue structure," *International Journal of Heat and Mass Transfer,* vol. 95, pp. 843-852, 2016.

[53] N. Kakuta, S. Yokoyama and K. Mabuchi, "Human thermal models for evaluating infrared images," *IEEE Engineering in Medicine and Biology Magazine,* vol. 21, no. 6, pp. 65-72, 2002.

[54] E. Kaltenbacher and R. C. Hardie, "High resolution infrared image reconstruction using multiple, low resolution, aliased frames," in *Proceedings of the IEEE 1996 National Aerospace and Electronics Conference NAECON 1996*, Dayton, 1996.

[55] M. S. Alam, J. G. Bognar, R. C. Hardie and B. J. Yasuda, "Infrared image registration and high-resolution reconstruction using multiple translationally shifted aliased video frames," *IEEE Transactions on instrumentation and measurement,* vol. 49, no. 5, pp. 915-923, 2000.

[56] M. Clinical, "CT scan," Mayo Clinical, 9 May 2018. [Online]. Available: https://www.mayoclinic.org/tests-procedures/ct-scan/about/pac-20393675. [Accessed 3 November 2019].

[57] B. P. Medoff, W. R. Brody, M. Nassi and A. Macovski, "Iterative convolution backprojection algorithms for image reconstruction from limited data," *JOSA,* vol. 73, no. 11, pp. 1493-1500, 1983.

[58] J. A. Reeds and L. A. Shepp, "Limited angle reconstruction in tomography via squashing," *IEEE transactions on medical imaging,* vol. 6, no. 2, pp. 89-97, 1987.

[59] X. Jin, L. Li, Z. Chen, L. Zhang and Y. Xing, "Anisotropic total variation for limited-angle CT reconstruction," in *IEEE Nuclear Science Symposuim & Medical Imaging Conference*, 2010.

[60] Z. Chen, X. Jin, L. Li and G. Wang, "A limited-angle CT reconstruction method based on anisotropic TV minimization," *Physics in Medicine & Biology,* vol. 8, no. 7, p. 2119, 2013.

[61] "Positron Emission Tomography - Computed Tomography," RadiologyInfo.org, 1 August 2019. [Online]. Available: https://www.radiologyinfo.org/en/info.cfm?pg=pet. [Accessed 3 November 2019].

[62] J. G. Rogers, R. Harrop and P. E. Kinahan, "The theory of three-dimensional image reconstruction for PET," *IEEE transactions on medical imaging,* vol. 6, no. 3, pp. 239-243, 1987.

[63] P. E. Kinahan and J. G. Rogers, "Analytic 3D image reconstruction using all detected events," Triumf, 1988.

[64] M. Defrise, D. W. Townsend and R. Clack, "Three-dimensional image reconstruction from complete projections," *Physics in Medicine & Biology,* vol. 34, no. 5, p. 573, 1989.

[65] T. S. Baker, W. W. Newcomb, N. H. Olson, L. M. Cowsert, C. Olson and J. C. Brown, "Structures of bovine and human papillomaviruses. Analysis by cryoelectron microscopy and three-dimensional image reconstruction," *Biophysical journal,* vol. 60, no. 6, pp. 1445-1456, 1991.

[66] T. Ekeberg, M. Svenda, C. Abergel, F. R. N. C. Maia, V. Seltzer, J.-M. Claverie, M. Hantke, O. Jönsson, C. Nettelblad, G. Van Der Schot and others, "Three-dimensional reconstruction of the giant mimivirus particle with an x-ray free-electron laser," *Physical review letters,* vol. 114, no. 9, p. 098102, 2015.

[67] A. Koulaouzidis and A. Karargyris, "Three-dimensional image reconstruction in capsule endoscopy," *World journal of gastroenterology: WJG,* vol. 18, no. 31, p. 4086, 2012.

[68] K. Wang, R. Su, A. A. Oraevsky and M. A. Anastasio, "Investigation of iterative image reconstruction in three-dimensional optoacoustic tomography," *Physics in Medicine & Biology,* vol. 57, no. 17, p. 5399, 2012.

[69] L. Mosser, O. Dubrule and M. J. Blunt, "Reconstruction of three-dimensional porous media using generative adversarial neural networks," *Physical Review E,* vol. 96, no. 4, p. 043309, 2017.

[70] C. Egger, J. von Wolfersdorf and M. Schnieder, "Combined Experimental/Numerical Method Using Infrared Thermography and Finite Element Analysis for Estimation of Local Heat Transfer Distribution in an Internal Cooling System," *Journal of Turbomachinery,* vol. 136, no. 6, p. 061005, 2014.

[71] I. Perez-Raya and S. G. Kandlikar, "Discretization and implementation of a sharp interface model for interfacial heat and mass transfer during bubble growth," *International Journal of Heat and Mass Transfer,* vol. 116, pp. 30-49, 2018.